Title

Compressive vs. tensile yield and fracture toughness behavior of a body-centered cubic refractory high-entropy superalloy Al0.5Nb1.25Ta1.25TiZr at temperatures from ambient to 1200°C

Authors

Kumar, Punit
Kim, Sang Jun
Yu, Qin
et al.

Publication Date

2023-02-01

DOI

10.1016/j.actamat.2022.118620

Acta Materialia 245 (2023) 118620

Contents lists available at ScienceDirect

Acta Materialia

journal homepage: www.elsevier.com/locate/actamat

Full length article

Compressive vs. tensile yield and fracture toughness behavior of a body-centered cubic refractory high-entropy superalloy $Al_{0.5}Nb_{1.25}Ta_{1.25}TiZr$ at temperatures from ambient to 1200°C

Punit Kumar [a,1], Sang Jun Kim [b,1], Qin Yu [a,1], Jon Ell [a,c], Mingwei Zhang [a,d], Yang Yang [a,d], Ji Young Kim [b], Hyung-Ki Park [e], Andrew M. Minor [c,d], Eun Soo Park [b,**], Robert O. Ritchie [a,c,*]

[a] Materials Sciences Division, Lawrence Berkeley National Laboratory, Berkeley, CA, USA
[b] Department of Materials Science and Engineering, Research Institute of Advanced Materials & Institute of Engineering Research, Seoul National University, Seoul, Republic of Korea
[c] Department of Materials Science and Engineering, University of California, Berkeley, CA, USA
[d] National Center for Electron Microscopy, Molecular Foundry, Lawrence Berkeley National Laboratory, Berkeley, CA, USA
[e] Functional Materials and Components R&D Group, Korea Institute of Industrial Technology, Gangneung, Republic of Korea

ARTICLE INFO

Keywords:
Multiple principal element alloys
Superalloys
Refractory alloys
High-temperature deformation
Tensile behavior
Intergranular fracture

ABSTRACT

The microstructure of high-entropy alloys with refractory elements and Al as constituents can be considered to be analogous to superalloys. These so-termed refractory high-entropy superalloys (RHSAs) can show remarkable compressive strength up to temperatures exceeding 1200 °C. Here, we examine the microstructure and properties - compressive, tensile, and fracture toughness - of a precipitation-hardened, body-centered cubic, RHSA, $Al_{0.5}Nb_{1.25}Ta_{1.25}TiZr$, at ambient temperature (RT) to 1200 °C. Two dual-phase microstructures comprising ordered B2 (brittle) and disordered A2 (ductile) phases were produced in this alloy - one with B2 as the matrix, the other with A2 - for evaluation of the mechanical properties. Under compression, both microstructures display RT compressive strengths above 1.5 GPa and considerable ductility exceeding 40% at elevated temperatures; the alloy with the A2 matrix has ~15% compressive ductility even at RT. However, properties are very different under tensile loading; at all temperatures, both microstructures fail predominately in an intergranular mode in the elastic regime at a fracture stress less than 200 MPa and ductility below 0.15%. The microstructure with the A2 matrix has a K_{Ic} fracture toughness of ~15 MPa$\sqrt{m}$ at RT, although at all temperatures above 800 °C, measured K_{Ic} values for both dual-phase microstructures are less than 5 MPa$\sqrt{m}$. In this study, we investigate the microstructural origin of these mechanical properties, and emphasize the importance of evaluating these alloys in tension.

1. Introduction

The quest for stronger and tougher structural materials is challenging because of the mutually exclusive nature of strength and ductility [1,2]. Additionally, for high-temperature applications such as future turbine engines and hypersonic vehicles, where materials are exposed to extreme environmental conditions, oxidation and stress-corrosion resistance requirements add to the complexity of materials selection and design [3,4]. Multiple principal element alloys, such as refractory high-entropy alloys (RHEAs), sometimes termed refractory complex-concentrated alloys, that have been developed as a subset of the high-entropy alloy concept [5–7], can potentially be suitable for these applications. This is evident because a vast compositional space exists for the development of new RHEAs that allows tailoring of properties ideal for high-temperature applications [8]. Moreover, a few of the already developed alloys have higher specific strengths than the present Ni-base superalloys at temperatures used for these applications [9,10], and RHEAs are expected to show relatively higher creep resistance owing to their high melting temperatures and the sluggish diffusion of their constituent elements [8–10].

* Corresponding author at: Department of Materials Science and Engineering, Berkeley, California.
** Corresponding author at: Department of Materials Science and Engineering at Seoul National University
E-mail addresses: espark@snu.ac.kr (E.S. Park), ritchie@berkeley.edu (R.O. Ritchie).
[1] These authors contributed equally to this work.

https://doi.org/10.1016/j.actamat.2022.118620
Received 9 July 2022; Received in revised form 10 December 2022; Accepted 12 December 2022
Available online 13 December 2022

So called refractory high-entropy superalloys (RHSAs) are a relatively new class of RHEAs that can potentially demonstrate all the properties mentioned above. Moreover, although the crystal structures are different, the microstructures of such RHSAs are analogous to the $\gamma + \gamma'$ microstructures in Ni-base superalloys; specifically, they typically involve a combination of ordered (B2) and disordered (A2) body-centered cubic (*bcc*) phases, where one phase is in the form of nanometer-size cuboidal precipitates that are atomically coherent with a narrow channel of surrounding matrix phase [11]. $AlMo_{0.5}NbTa_{0.5}TiZr$, $Al_{0.3}NbTaTi_{1.4}Zr_{1.3}$, and $Al_{0.5}NbTa_{0.8}Ti_{1.5}V_{0.2}Zr$ represent a few of the originally developed RHSAs [11,12]. In as-processed conditions, specifically after a standard homogenization treatment at 1400 °C followed by short-term aging at 600 °C (~0.5 h), the microstructures of these alloys consist of cuboid precipitates of A2 distributed in ordered B2 matrix [12,13]. Since the hard B2 phase is the matrix, these alloys show compressive yield strengths (σ_Y^c) ≥2000 MPa at room temperature (RT) and ≥700 MPa up to 1000 ℃ [11,12], but with limited ductility at RT even in compression. Nevertheless, the RT plastic response of RHSAs in compression can be improved by heat treatment in the miscibility gap to induce microstructural inversion, *i.e.*, the formation of a basket weave structured A2 matrix with B2 cuboid precipitates. Indeed, this can lead to significant plasticity (in compression) at RT and above [13,14], but can also result in a reduction in strength [14]. Despite this, compared to other high-temperature structural alloys such as Ni and Co-based superalloys, RHSAs do in general maintain their high compressive strength up to 1200 °C [12].

However, recent studies have highlighted the microstructural instability of certain RHSAs during deformation at temperatures as low as 600 °C [15,16]. During long-term high-temperature exposure, additional phases can form as well as the A2 and B2 phases [16,17]; for example, Al-Zr rich precipitates that decorate the grain boundaries (GBs) are a particular problem in these alloys [16,17]. Of further concern is that, to date, the mechanical properties of RHSAs have invariably been investigated in compression [9,11]. While such testing can provide useful information on the deformation properties, the failure of a material in compression is far less sensitive to microstructural imperfections and processing-induced flaws, which can lead to catastrophic failures under tension. Moreover, structural materials must show sufficient strength and ductility in tension and display adequate fracture toughness for the vast majority of safety-critical applications [2,9,18].

Accordingly, in this work, our prime objective is to examine the mechanical behavior of an $Al_{0.5}Nb_{1.25}Ta_{1.25}TiZr$ RHSA in tension as well as compression and specifically to determine its fracture toughness properties over the temperature range from RT to 1200 °C. To this end, the alloy was processed with two initial dual-phase (A2 + B2) microstructures that were expected to exhibit relatively high ductility and strength in compression: one with (ductile) A2 precipitation within a (brittle) B2 matrix, the second with B2 precipitation within an A2 matrix. Our specific focus here is: (i) whether microstructural design to generate improved plasticity (ε_f^c) under compressive loading translates into the improved tensile ductility (ε_f) at ambient temperatures, (ii) whether this can be also achieved at elevated temperatures, (iii) what the effects may be of thermally unstable microstructures on the uniaxial tensile and fracture toughness properties of this RHSA at elevated temperatures, and (iv) an overall assessment of the ambient to elevated temperature mechanical performance of these alloys.

2. Materials and experimental procedures

2.1. Materials

Ingots of $Al_{0.5}Nb_{1.25}Ta_{1.25}TiZr$, which is $Al_{10}Nb_{25}Ta_{25}Ti_{20}Zr_{20}$ in at. %, were fabricated by vacuum arc melting of individual high purity elements of Al, Nb, Ta, Ti, and Zr. The as-cast ingots were remelted in the arc melter five times to ensure a homogeneous composition. Subsequently, the ingots were hot isostatic pressed (HIP) at 1500 °C using a pressure of 200 MPa for 2 h and heat-treated following the processing steps illustrated in Fig. 1. To avoid oxidation and contamination, the HIP and heat-treatment processes were carried out in an inert Ar atmosphere and vacuum, respectively. Before the final aging treatment at 800 ℃ for 12 h followed by air-cooling, the ingots were electrical discharge machined (EDM) into 3 mm plates. This microstructure is hereafter referred to as HT800. The plates were then machined into the final shapes of dog-bone-shaped uniaxial tensile, cylindrical compression, and compact-tension (C(T)) fracture toughness specimens to characterize mechanical properties. Half of the plates were re-homogenized at 1300 °C for 12 h, then aged at 600 °C for 24 h, and air-cooled, then machined into the final specimens with complementary microstructure. This latter microstructure is referred to as HT600, a nomenclature reflecting the aging treatment at 600 °C. The compositions of both HT600 and HT800 microstructures are listed in Table 1.

2.2. Experiments

Metallographic samples were mechanically mirror polished for microstructural characterization by back-scattered electron (BSE) imaging in a scanning electron microscope (SEM; MIRA3, Tescan). Also, electron backscatter diffraction (EBSD; eFlash FS, Bruker) based inverse pole figures (IPF) and energy dispersive spectroscopy (EDS) maps were obtained to analyze the phase constitution, grain size, and texture of the material. High-resolution transmission electron microscopes (TEM) FEI Tecnai G2 Spirit TWIN, FEI TitanX, and a JEOL JEM-2010F were used to investigate relatively small micro- and nano-scale microstructural features. Thin foil TEM specimens were prepared by dry mechanical grinding followed by ion milling from blocks of the HT600 and HT800 materials before and after their deformation. The phase composition of the HT600 and HT800 specimens was characterized by X-ray diffraction (XRD; D2 PHASER, Bruker) using monochromatic Cu Kα with a scanning rate of 4°/min. For the HT600 and HT800 microstructures, interstitials (C, N, and O) were characterized by LECO (ONH836 and CS844 models), which uses inert gas fusion procedures for O and N detection and combustion infrared for C detection. Five specimens, weighing 0.1–0.5 g, were sectioned from the bulk material for both microstructural conditions.

To analyze the mechanical behavior by compression, tensile, and fracture toughness tests, the HT600 and HT800 specimens were machined into the uniaxial tension, compression, and compact-tension (C(T)) geometries illustrated in Fig. S1 of the Supplementary Information. All the mechanical tests were performed on an automated MTS 810 servo-hydraulic testing machine equipped with an Instron 8800 controller. Cylindrical compression samples of diameter ~4 mm and height of ~8 mm were deformed between SiC platens in a fixture mounted on the servo-hydraulic testing machine. Compression tests on the HT600 and HT800 specimens were carried out in displacement

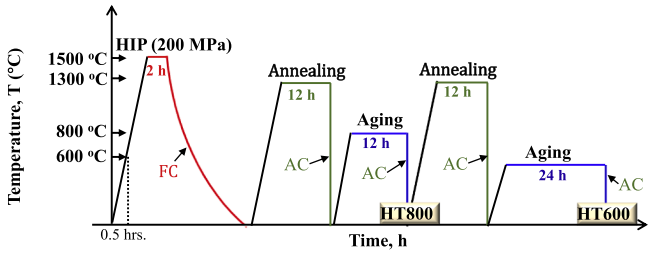

Fig. 1. Schematic illustration of the processing steps utilized to fabricate the specimens used in the present study. Here HT600 and HT800 represent the microstructures produced by final aging treatments at 600 and 800 °C, respectively. The specimens were machined into their final shapes for compression, tension, and fracture toughness tests before the final aging step. FC and AC refer to furnace and air cooling, respectively.

Table 1
Composition of $Al_{0.5}Nb_{1.25}Ta_{1.25}TiZr$ RHSA.

Elements	HT600 (wt.%)	HT600 (at.%)	HT800 (wt.%)	HT800 (at.%)
Nb	22.9 ± 0.6	24.8	22.1 ± 0.1	23.6
Ta	48.1 ± 0.7	26.8	47.3 ± 0.1	25.9
Ti	9.3 ± 0.2	19.6	9.6	19.9
Zr	17.5 ± 0.6	19.3	18.5 ± 0.1	20.1
Al	2.2 ± 0.1	8.2	2.4	8.8
C	0.018 ± 0.005	0.15	0.023 ± 0.008	0.19
N	0.034 ± 0.003	0.24	0.123 ± 0.08	0.87
O	0.143 ± 0.025	0.9	0.12 ± 0.02	0.74

control with a constant crosshead speed of ~0.2 mm/min, corresponding to a strain rate of 4×10^{-4} s^{-1}. If the specimens did not fracture during compression loading, the tests were stopped after a 40% reduction in the height of the specimens. Uniaxial tensile tests on both HT conditions were performed using dog-bone-shaped specimens with a thickness, width, and gage length of 3, 2, and 10 mm, respectively. The tensile tests were performed following the procedure recommended in ASTM E8 [19] using a relatively slow strain rate of $\sim 3.3 \times 10^{-4}$ s^{-1} because of the brittle nature of these specimens. True stress-strain (σ-ε) values measured in the compression and tension tests are reported in the stress-strain plots after compliance correction. For the fracture toughness tests, C(T) specimens, with a width of ~18 mm and thickness of 4.5 mm, were machined from the material blocks of both HT conditions. The C(T) specimens were micro-notched to form a sharp crack tip instead of fatigue precracking to avoid sudden brittle fracture of the material during fatigue loading in the presence of a crack. The C(T) specimens were first notched using a low-speed diamond saw and then sharpened using a micro-notcher to achieve the total crack length (a_o) ~9 mm, which corresponds to a_o/W ~0.5 as recommended in ASTM E399 [20] (W is the specimen width). The radius micro notcher uses a thin razor blade covered in 5 μm diamond polishing paste under a compression load to create a very sharp notch in the specimens. The final notch root radii of all the C(T) specimens were <20 μm. After notching, the specimens were loaded in quasi-static mode until fracture at a displacement rate of 0.2 mm/min to determine the mode-I fracture toughness (K_{Ic}) in accordance with ASTM Standard E1820 [21]. To satisfy the plane strain and the small-scale yielding criteria as recommended in the Standard, a dimension defined as ~15 times the size of the plastic-zone size, $L \sim 2.5 (K_{Ic}/\sigma_y^c)^2$, should be less than the thickness (4.5 mm) and the uncracked ligament size (W-$a \approx 9$ mm) of the C(T) specimens; here K_{Ic} and σ_y^c are the fracture toughness and compressive yield strength of the specimens in respective testing conditions. In present case, the maximum L (~5.45 mm) was measured for HT600 specimen tested at 1200 °C, although, in all other cases, L is <4.5 mm, *i.e.*, smaller than the thickness and the uncracked ligament size of the C(T) specimens.

All mechanical tests were performed at RT (~25 °C), 800 °C, 1000 °C, and 1200 °C. A high-temperature resistance furnace (MTS 657.01) was used for conducting the elevated temperature tests. To accurately measure the temperature during the tests to ensure uniform heating, two K-type thermocouples were spot-welded directly to the top and bottom of the dog bone tensile specimens (just outside the gage length) and at the edges of the C(T) fracture toughness specimens; however, only one thermocouple was attached to the compression samples because of their relatively small size. For the mechanical testing, an average heating and cooling rate of 20 and 25 °C/min were used. The specimen was kept at the testing temperature for 20 mins to homogenize before performing the mechanical tests. Since the refractory high-entropy superalloy (RHSA) can quickly oxidize at such high temperatures, a tube was inserted into the center of the furnace that was flooded with a constant flow of Ar gas to reduce the oxidation of the specimens during heating, testing, and cooling back to ambient conditions.

Fractography of the failed tensile and C(T) specimens was carried out using scanning electron microscopy. The samples were sectioned from the undeformed regions (grip section) of the tensile coupons and examined by SEM and EDS to understand the effect of temperature on the evolution of microstructure. To investigate the deformation mechanisms, the gage sections of the HT600 and HT800 tensile coupons tested at 1000 °C were machined from the center to expose the representative deformed regions near the fracture surface. Since all the specimens were quenched by Ar gas after the tests, microstructural changes can be presumed to be minimal during the cooling process. *Post facto* nano-indentation tests were carried out on the HT800 microstructure to investigate the hardness of the different phases. The nano-indentation tests were performed using a trapezoidal load function of peak load ~3000 μN and a creep hold of ~40 s, with loading and unloading rates of ~600 μN/s. A spherical diamond tip diameter of 1 μm was used for all the nano-indentations.

3. Results

3.1. Microstructure

To identify the phases in the microstructure of the $Al_{0.5}Nb_{1.25}Ta_{1.25}TiZr$ RHSA, XRD was performed on both HT conditions; diffraction patterns are displayed in Fig. S2A. The diffraction peaks of this alloy correspond to two *bcc* phases, one is the disordered A2 phase, and the other is the ordered B2 phase. In the HT600 condition, the lattice parameter of the A2 phase was measured to be ~3.32 Å and that of the B2 phase as ~3.34 Å. The lattice parameter of the A2 phase remained unchanged (~3.32 Å) even after aging at 800 °C for 24 h; however, the lattice parameter of the B2 phase increased to ~3.42 Å (Fig. S2B–E). The growing lattice parameter of the B2 phase in the HT800 microstructure is possibly related to the change in the coherency of the A2 and B2 interface due to the coarsening of the phases during aging [22,23]. These microstructural changes during aging at 800 °C have also been reported in RHSAs with similar compositions [13–16]. Micrographs of the RHSA after the HT600 and HT800 heat treatments are displayed in Fig. 2. The microstructure of the HT600 specimens, shown in Fig. 2A as a high-angle annular dark-field scanning transmission electron microscopy (HAADF-STEM) image, consists of an ordered B2 phase with dark contrast forming a continuous channel analogous to a basket-weave structure embedded with disordered A2 cuboids as precipitates. The fine basket-weave microstructure with B2 as the matrix and A2 as the precipitates is more clearly illustrated in a dark-field TEM image of Fig. 2C, along with the diffraction pattern of the B2 phase from the [001] zone axis. Similar microstructures for other RHSAs have been reported to provide relatively higher RT compressive strength, σ_Y^c, due to the strong and brittle nature of the B2 matrix [11,14].

However, aging this RHSA in the miscibility gap can result in phase inversion, *i.e.*, B2 precipitates in the A2 matrix [14,15]. In the present study, this microstructural inversion was achieved by the HT800 treatment. The SEM back-scattered electron (BSE) image of the HT800 condition in Fig. 2B shows dark B2 precipitates distributed in the continuous A2 matrix (light contrast). The presence of B2 precipitates in the A2 matrix was confirmed by dark-field TEM imaging (Fig. 2D), along with the diffraction pattern of the B2 phase from the [110] zone axis. In certain regions of the HT800 structure, abnormal growth of the B2 phase can also be observed. The A2 phase, as compared to B2, has a relatively higher composition of the high atomic number elements Nb and Ta; therefore, the A2 phase looks brighter in the BSE-SEM images [24]. Since the microstructure in the HT800 condition has the A2 phase as the matrix where A2 is relatively more ductile compared to B2 [14], the RT ductility of the HT800 condition is expected to be somewhat higher, at least in compression. Consequently, the complementary microstructures obtained by HT600 and HT800 treatments provide an opportunity for a comprehensive investigation into the range of mechanical properties of this RHSA.

The micrograph of HT600 specimen displayed in Fig. 3A shows oval-shaped dark precipitates of a size ~1.8 ± 0.7 μm distributed along the

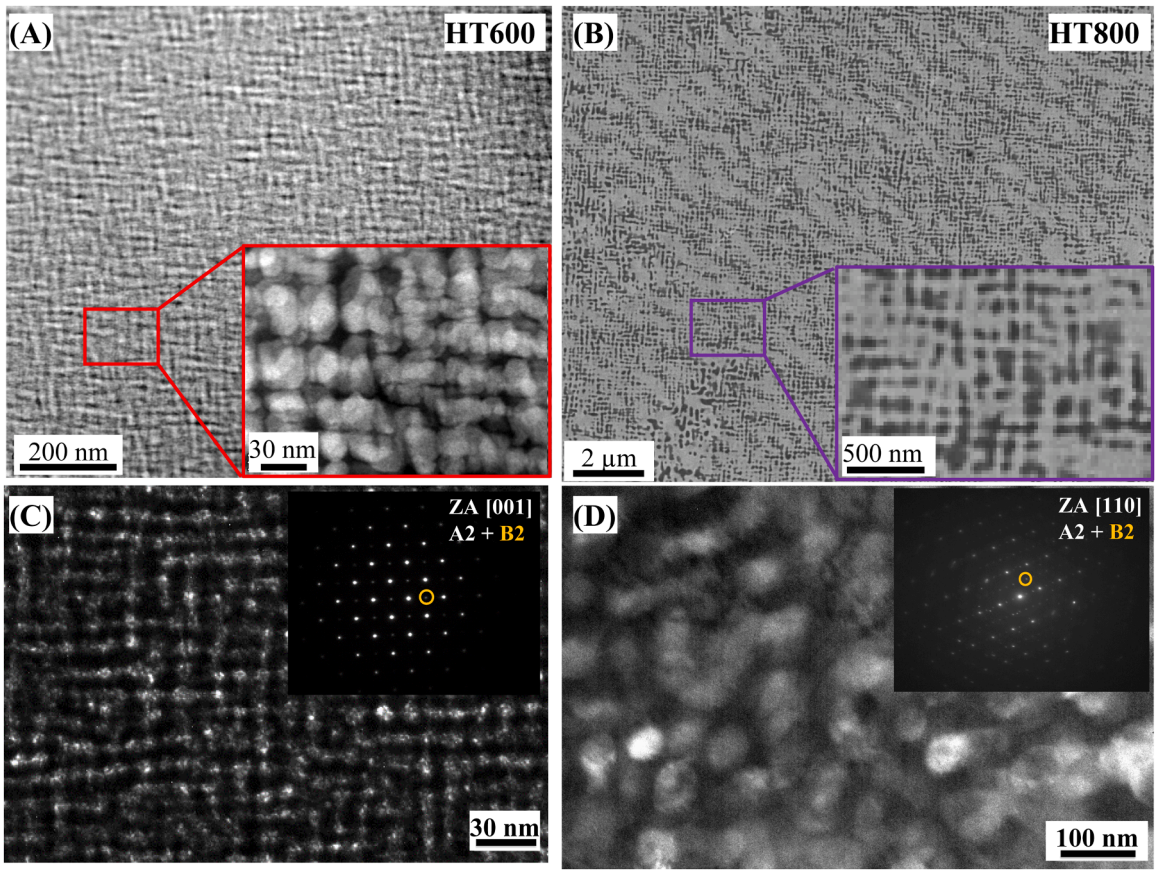

Fig. 2. Representative microstructures of RHSA specimens in (**A**) HT600 condition obtained by high-angle annular dark-field scanning transmission electron microscopy (HAADF-STEM), and (**B**) HT800 condition obtained by back-scattered electron microscopy. The images in the inset of **(A)** and **(B)** show high magnification images from the locations indicated in the respective images. **(C)** TEM dark-field image of the HT600 condition from [001] zone axis, and **(D)** TEM dark-field image of the HT800 condition from [110] zone axis. The diffraction patterns in the inset of **(C)** and **(D)** show the spots of both the A2 and B2 (orange circle) phases.

grain boundaries with rod-shaped precipitates (of similar dark contrast) randomly scattered inside the grains. Previous studies on RHSAs have reported presence of precipitates with similar morphologies [16,17]. These precipitates were identified to be Al-Zr rich intermetallics by TEM EDS (Fig. S3). As shown in Fig. 3B, they are connected by a thin layer of the same intermetallic phase of thickness (t) ~50 ± 8 nm growing along the grain boundaries. Such a thin grain-boundary layer of Al-Zr precipitates with a serrated morphology has been reported in other RHSAs annealed at 1400 °C [16]. In our HT800 microstructure, the oval-shaped Al-Zr rich precipitates can be seen to be randomly distributed inside the grains (Fig. 3C). The precipitates distributed on the grain boundaries are relatively fine, *i.e.*, ~0.42 ± 0.22 μm in size, but are fragmented into small rods or oval shapes (Fig. 3D). In the HT600 microstructures, grain-boundary precipitates are also Al-Zr rich intermetallics. However, as Al and Zr are additionally important atomic constituents of the B2 precipitates [25], the occurrence of the grain-boundary precipitation results in the formation of precipitate-free zones (PFZ) adjacent to the boundaries, as indicated by the white arrows in Fig. 3B and D. The half width of these PFZs (W_{PFZ}) were found to be 0.061 ± 0.017 and 0.67 ± 0.16 μm in HT600 and HT800 microstructures, respectively.

3.2. Mechanical properties in compression

Fig. 4A and B show the compression stress-strain curves of the HT600 and HT800 specimens tested at RT, 800, 1000, and 1200 ℃. The following observations can be made from these tests: (i) Both the HT600 and HT800 specimens display plasticity at all the test conditions except the RT HT600 specimens that failed prior to general yield. (ii) Although the HT600 specimens exhibit no noticeable plasticity at RT, their average σ_Y^c is 28% higher than that of HT800, assuming the peak strength $\sigma_P \approx \sigma_Y^c$ for HT600; furthermore, at RT, the HT800 microstructure shows a 900% higher fracture strain in compression ($\varepsilon_f^c \approx 13\%$) compared to HT600 ($\varepsilon_f^c \approx 1.3\%$). (iii) In the temperature range of 800 – 1200 ℃, both the HT600 and the HT800 microstructures show similar compressive yield (σ_Y^c) and fracture (ε_f^c) strains.

During all high-temperature compression tests, the stress-strain curves show softening behavior after the flow stress reaches the peak strength σ_P. For example, at 1200 °C, after reaching σ_P, a steady-state flow stage with a constant slope was observed in the specimens from both conditions until the tests were stopped at a strain of ~35–40%. At 800 °C, the drop in flow stress after σ_P is much sharper compared to that at 1000 and 1200 °C. The marked differences in the flow behavior of the HT600 and HT800 specimens at 800 °C compared to 1000 and 1200 °C occur because these test temperatures expose the alloy to the multi-phase regions of their phase diagram. Such behavior has been observed in conventional alloy systems having two phases stable at relatively low temperatures. For example, in a near-α titanium alloy, the flow stress drops significantly after reaching the peak strength in the α+β two-phase temperature region (< 1045 °C), whereas above 1045 °C a steady-state flow stress is observed after the peak strength as the alloy is in the β phase temperature region [26,27]. Ni-base superalloys with characteristic γ + γ′ microstructures also show similar plastic flow behavior during high-temperature compression [28]. To deduce the solvus temperature of the RHSA used in the present study, the alloy was annealed at 1000 °C and 1200 °C for 24 h; the resulting microstructures are shown in Fig. S4. When the RHSA is annealed at 1000 °C, the B2 phase precipitates are distributed inside the A2 matrix (Fig. S4A); however, after annealing at 1200 °C, the microstructure consists of only

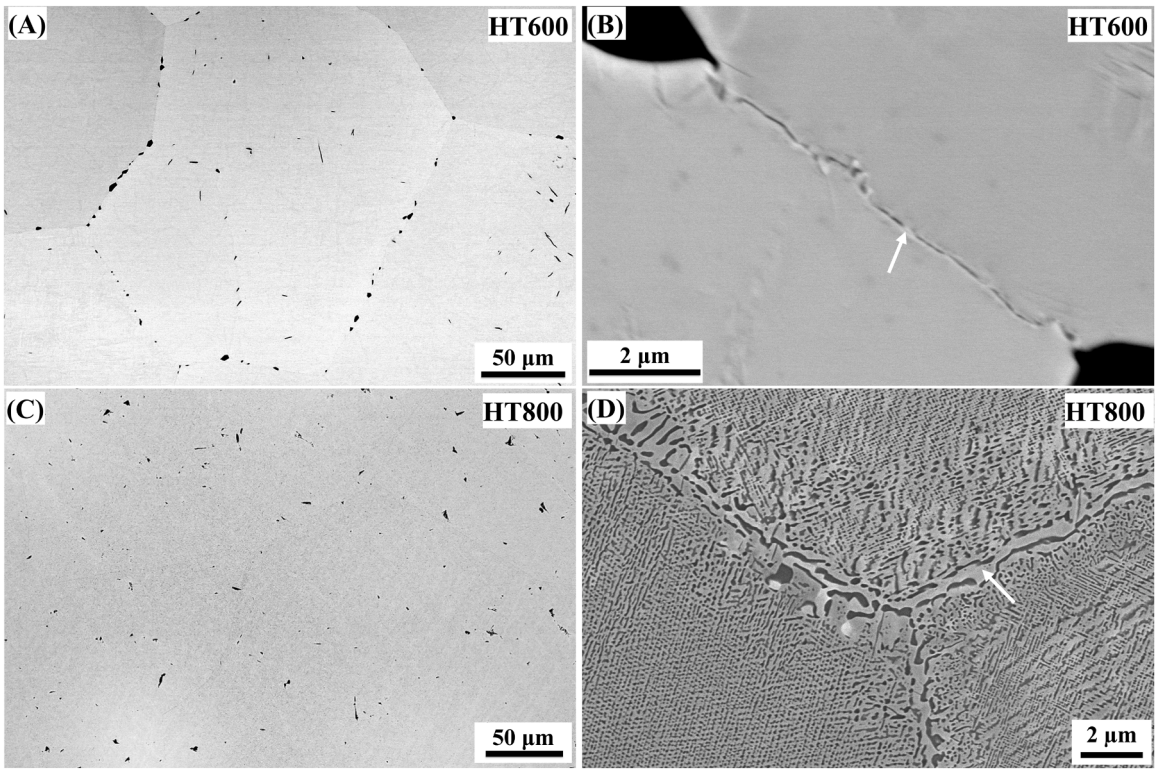

Fig. 3. Representative back-scattered electron images showing the presence of the grain boundary Al-Zr rich precipitates in **(A, B)** HT600, and **(C, D)** HT800 microstructures. The white arrows in Fig. **(B)** and **(D)** indicate precipitate-free zones (PFZs) in the respective microstructures.

the A2 phase (Fig. S4B). This confirms that the solvus temperature for phase transformation (A2+B2 → A2) lies between 1000 and 1200 °C.

Fig. 4C shows the effect of temperature on the compressive yield strength σ_Y^c of the present RHSA in comparison to data for other comparable RHEAs (VNbMoTaW [7], TiNbHfZrTa [29,30]) and RHSAs ($AlMo_{0.5}NbTa_{0.5}TiZr$ [12], $Al_{0.4}Hf_{0.6}NbTaTiZr$ [24]). The current HT600 microstructure displays the highest σ_Y^c at RT but shows brittle characteristics similar to the VNbMoTaW alloy. The σ_Y^c of the HT800 microstructure is ~2% lower than that for VNbMoTaW but 24% higher than in TiNbHfZrTa. However, at RT, the HT800 microstructures display ~10 times higher compressive ductility prior to failure compared to VNbMoTaW. At 800 °C, HT600 and HT800 microstructures display a similar σ_Y^c, which is 26% lower than the σ_Y^c of VNbMoTaW but 16% higher than in TiNbHfZrTa. Moreover, at 1000 and 1200 °C, HT600, HT800, and TiNbHfZrTa show similar compressive yield strengths σ_Y^c , which is less than half of that of VNbMoTaW. In comparison, the RHSA with Mo as one of the additional constituents, *i.e.*, $AlMo_{0.5}NbTa_{0.5}TiZr$, outperforms the RHSA microstructures investigated in the present study [12]. However, the σ_Y^c of $Al_{0.4}Hf_{0.6}NbTaTiZr$ is similar to that of HT600 microstructures at all temperatures [24]. Compared to the Ni-based superalloy Inconel 718, the RHSA shows a higher compressive strength at all tested temperatures [9].

3.3. Mechanical properties in tension

The corresponding uniaxial stress-strain properties of the HT600 and HT800 microstructures under tensile loading are displayed in Fig. 5. The following observations can be made from the results of the tensile tests: (i) For both microstructural conditions, minimal tensile ductility was observed at all temperatures; all the tensile specimens fractured with at a ductility ε_f in the range of ~0.01%–0.15%, prior to general yielding; these values are dramatically lower than those measured in compression. (ii) The maximum fracture strength (σ_f) was observed at RT; specifically, σ_f ≈110 and 188 MPa for the HT600 and HT800 microstructures, respectively (Fig. 5A and B). (iii) The fracture strength in tension σ_f of the HT800 microstructure at RT is 39% higher than that of the HT600 microstructure, which is quite different to the 28% higher σ_Y^c of the HT600 structure measured in compression. (iv) With increasing temperature, there is a significant decrease in the σ_f of both the HT600 and HT800 microstructures (Fig. 5C), although the HT800 structure retains its relatively higher tensile fracture strength σ_f up to 1200 °C. At 1200 ℃, both the HT600 and HT800 microstructures display very low fracture strengths σ_f ~15 and 24 MPa, respectively.

Specifically, the fracture strength σ_f values of the $Al_{0.5}Nb_{1.25}Ta_{1.25}$-TiZr RHSA measured for both microstructures and all testing conditions are ~77–95% lower in uniaxial tension than that observed in compression. Similarly, the RT ductility ε_f measured in uniaxial tension is 92.3% and 99% lower than the fracture strain in compression, respectively in the HT600 and HT800 microstructures. At temperatures above 800 °C, this difference in the tension vs. compression ductility is even larger; all specimens tested in compression survived strains exceeding 35% but fractured at strain less than 0.05% in tension.

The fracture of all tensile specimens in both microstructures at all temperatures can be seen in Fig. 6 to be fully intergranular. Some specimens also showed the presence of secondary cracks (marked by red squares in Fig. 6), which indicate where cracks may have initiated from processing flaws but did not propagate as their location was not favorably aligned with the mode-I loading direction. The very low ductilities ε_f in tension (plotted in Fig. 5, *c.f.*, Fig. 4) are certainly consistent with the sensitivity of high-strength, nominally brittle, alloys to pre-existing flaws or other microstructural imperfections, a critical property which is almost completely obscured when uniaxial stress-strain behavior is only measured in compression. However, the flaw-sensitivity that results in this marked difference in tension vs. compression constitutive behavior is somewhat less stark in the HT800 microstructure as the matrix is primarily the A2 phase which is less brittle than the B2 matrix of the HT600 structure.

To be fair, other high-temperature materials that have been

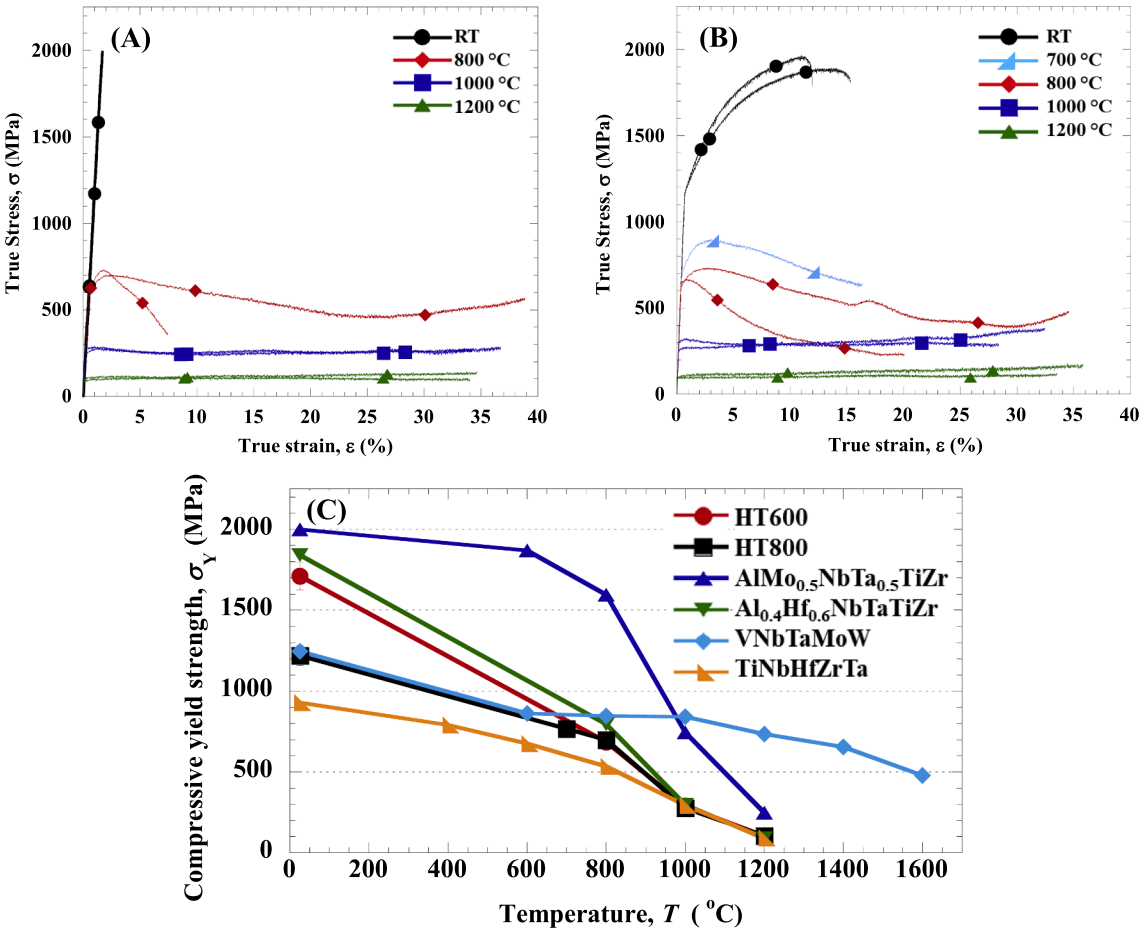

Fig. 4. Compression true stress-strain curves from the **(A)** HT600 and **(B)** HT800 microstructures tested at RT, 800 °C, 1000 °C, and 1200 °C. **(C)** Variation of the compressive yield strength of RHSA (HT600 and HT800) and other refractory high-entropy alloys/superalloys ($AlMo_{0.5}NbTa_{0.5}TiZr$ [12], $Al_{0.4}Hf_{0.6}NbTaTiZr$ [24], VNbMoTaW [7], TiNbHfZrTa [29,30]) with temperature.

contemplated as replacements to Ni-base superalloys can show brittle behavior under tensile loading. For example, Nb-Hf-Ti-Si silicide composites show significantly lower σ_f under the tensile compared to compression loading across the temperature range of RT to 1400 °C [31]. Furthermore, the Mo-8.9Si-7.7B alloy exhibits an ultimate tensile strength (σ_u) close to 400 MPa, which is very low compared to its σ_Y^c in temperature range RT to 1200 °C [32]. Intermetallic γ-TiAl alloys similarly have far higher compressive strengths; their tensile yield strength is typically σ_Y ~300 MPa at RT, which drops to 150 MPa at 1000 °C [33], whereas their compressive strength can be as high as 750 MPa up to 800 °C [27]. In addition to the difficulty of processing these alloys, their poor strength and especially ductility under tensile loading remain one of the most significant issues barring their replacement of Ni-base superalloys. A notable RHEA series, *i.e.*, variants of HfNbTaTiZr, show ~8–15% tensile ductility in the temperature range of −196 °C to 400 °C. To the best of our knowledge, however, the tensile properties of these RHEAs at temperatures ≥800 °C have not been investigated [34,35].

3.4. Fracture toughness

The determination of the plane-strain fracture toughness (K_{Ic}) of RHSAs and other refractory HEAs at higher temperatures (>800 °C) is essential for their potential adoption in most safety-critical structural applications. Our measurements of the effect of temperature on the fracture toughness of both HT600 and HT800 microstructures show that, analogous to the poor tensile ductility of these alloys, the K_{Ic} values are lower than 15 MPa$\sqrt{m}$ for all conditions (Fig. 7). Specifically, at RT, the fracture toughness of the HT800 microstructure (~14.4 MPa$\sqrt{m}$) is almost 5 times higher than that of the HT600 microstructure (~3.1 MPa$\sqrt{m}$). However, at higher temperatures (800 to 1200 °C), the toughness of both microstructures is very low (K_{Ic} < 5 MPa$\sqrt{m}$).

To compare with other high-temperature materials, the value of K_{Ic} for the present $Al_{0.5}Nb_{1.25}Ta_{1.25}TiZr$ RHSA is only 15% of that of the single-crystal Ni-base superalloy Rene-N5 at RT and even lower at 800 °C (Fig. S5) [36]. Compared to Nb-Hf-Ti-Si silicide composites, however, the RT K_{Ic} of the HT800 microstructure is slightly higher, although the toughness of the silicide remains essentially constant (≤10 MPa$\sqrt{m}$) up to 1100 °C [31]. γ-titanium aluminide intermetallics exhibit a similar RT K_{Ic} ≤10 MPa$\sqrt{m}$, but this can be improved to 40 MPa$\sqrt{m}$ depending on the orientation of the $\alpha_2(Ti_3Al)/\gamma$ lamellar in the microstructure with respect to the crack growth direction [37]; furthermore, unlike the RHSA, the toughness of γ-titanium aluminides is comparatively insensitive to temperature [38]. Most other refractory alloys and intermetallics, such as Mo alloys and NiAl, similarly have toughnesses less than ~10 MPa$\sqrt{m}$ [39]); the K_{Ic} of the present HT800 microstructure RHSA (HT800) is ~50% higher at RT, although it drops substantially at temperatures of 800 to 1200 °C.

EBSD inverse pole figure (IFP) maps which track the crack path in the fracture toughness specimens of the HT600 microstructure tested at all temperatures are shown in Fig. 8; white arrows in the figures indicate the notch tip of the C(T) specimens. Similar to the tensile samples, the fracture toughness samples failed largely in an intergranular manner; similar results were found for the HT800 structure (Fig. S6), although limited transgranular fracture was apparent in the HT600 samples at RT (Fig. 8). Such a predominant intergranular fracture mode indicates that

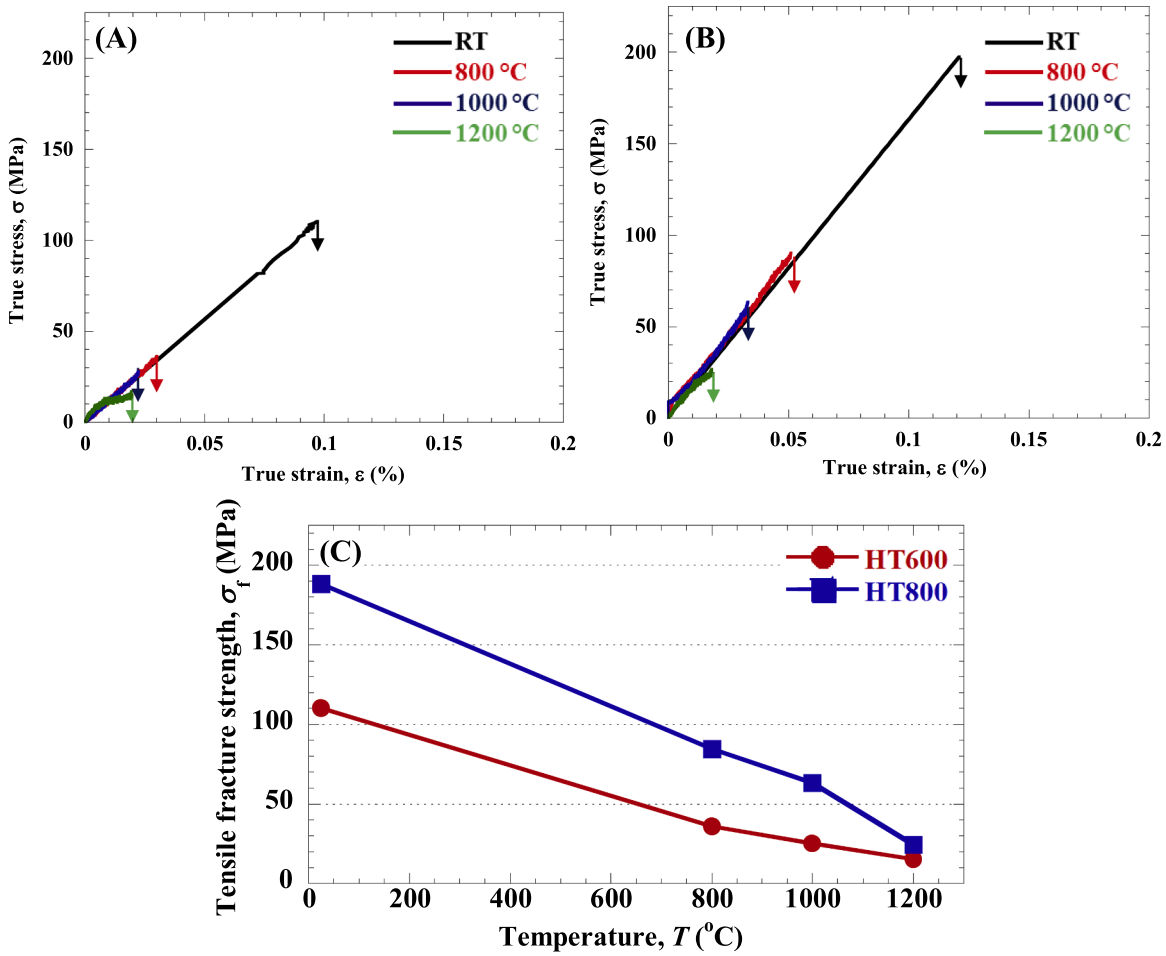

Fig. 5. Tensile true stress-strain curves of (**A**) HT600 and **(B)** HT800 specimens from tensile tests at RT, 800 °C, 1000 °C, and 1200 °C. (**C**) Variation of the tensile fracture strength with temperature for HT600 and HT800 specimens.

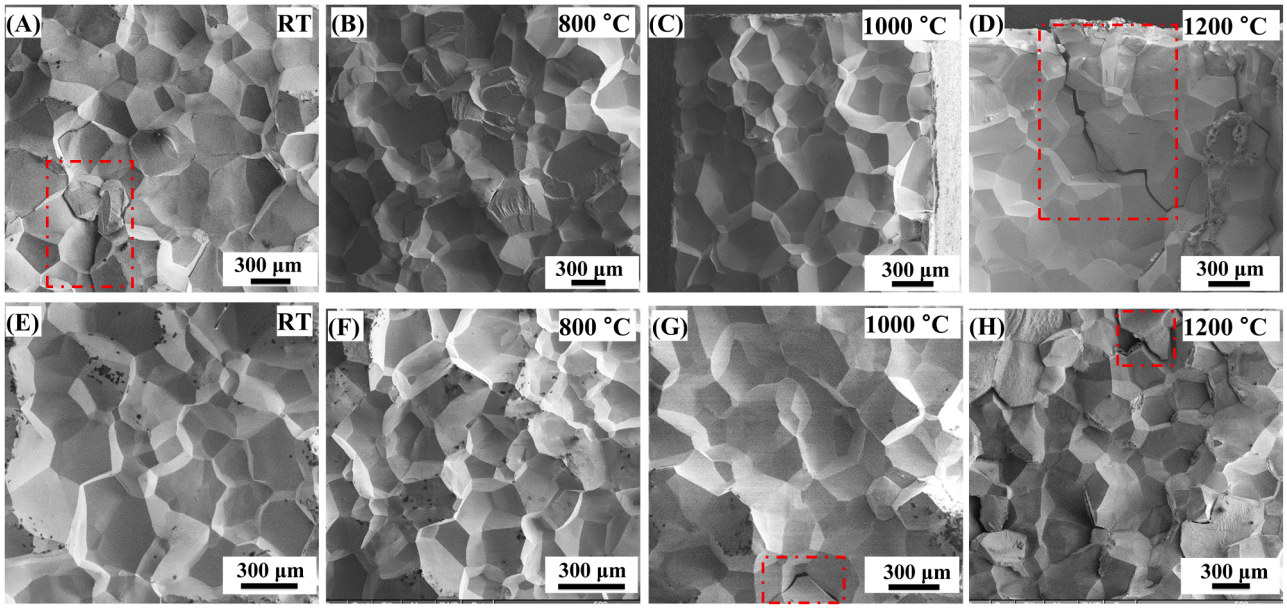

Fig. 6. Representative SEM images of the fracture surface of tensile specimens tested at RT, 800 °C, 1000 °C, and 1200 °C. Fig. **A**–**D** are for the HT600 microstructure, and **E** to **H** are for HT800 microstructure tested at respective temperatures indicated in the image**.** All samples exhibit fully intergranular fracture, although there is limited evidence of transgranular fracture in the HT600 structure at room temperature. The boxes marked by red dashed lines indicate regions where there is evidence of secondary cracks.

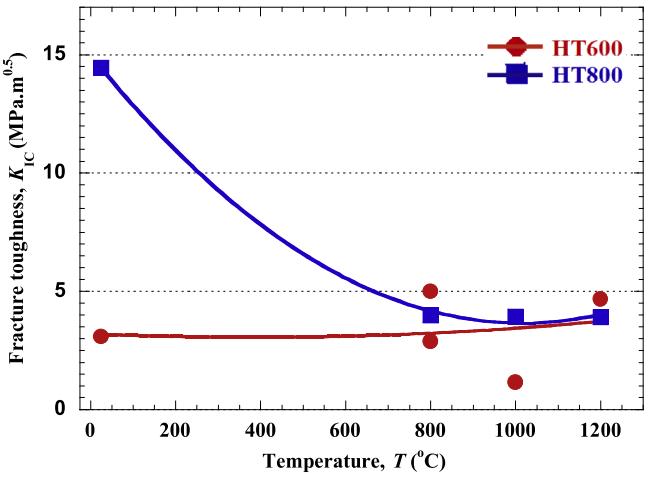

Fig. 7. Variation in the K_{Ic} fracture toughness with temperature for the HT600 and HT800 microstructures.

the boundaries cannot sustain sufficient strain to allow plastic deformation inside the grain under tensile loading; the possible reasons for this behavior are discussed in the following sections.

4. Discussion

4.1. Deformation mechanisms

One major finding of this study is that at temperatures above 800 °C, the $Al_{0.5}Nb_{1.25}Ta_{1.25}TiZr$ RHSA displayed fracture strains that exceeded 35% when tested in compression, whereas in uniaxial tension, these failure strains were reduced to less than 0.15%. In light of this over two orders of magnitude difference in ductility, *post facto* microstructural examination was conducted to understand the deformation mechanisms in compression and tension. Fig. 9 shows the EBSD IPF maps and a Kernel average misorientation (KAM) map of the HT600 specimens deformed at 1000 °C and 1200 °C, respectively. For compressive deformation at 1000 °C, the strain is uniformly distributed throughout the entire grain, but with some degree of dynamic recrystallization inside the grain and along the grain boundaries, as shown in Fig. 9A–C. The size of the recrystallized grains in the vicinity of the grain boundaries is ~1–2 μm. In contrast, at 1200 °C the strain is primarily localized along the boundaries where the strain map resembles a necklace, as illustrated by the KAM map in Fig. 9E, A high magnification IPF map in Fig. 9F shows relatively larger recrystallized grains (~3–4 μm) along the grain boundaries at this higher temperature with negligible recrystallization inside the grains. Such necklace structures of discontinuous dynamic recrystallized grains are usually observed when the deformation is localized at the grain boundaries; these phenomena have been reported in other compositions of RHSAs as well as HfNbTaTiZr and MoNbHfZrTi RHEAs during deformation at elevated temperatures [24,40,41].

To comprehend these local changes in microstructure, it is necessary to understand the evolution of the A2 and B2 phases with temperature and deformation. Fig. 10A–C show high magnification BSE images of the HT600 structure deformed in compression, respectively at 800 °C, 1000 °C, and 1200 °C. In all cases, the A2 and B2 phases grow in a direction aligned at ~45° to the compression direction, *i.e.*, in the direction of the maximum shear stress. This is similar to the rafting phenomenon observed in Ni- and Co-base superalloys [42–44]. Further, they are similar to the microstructure of the undeformed HT800 RHSA displayed in Fig. 2B, where B2 is precipitated in the A2 matrix. The phase inversion was accelerated under the compressive stress at high

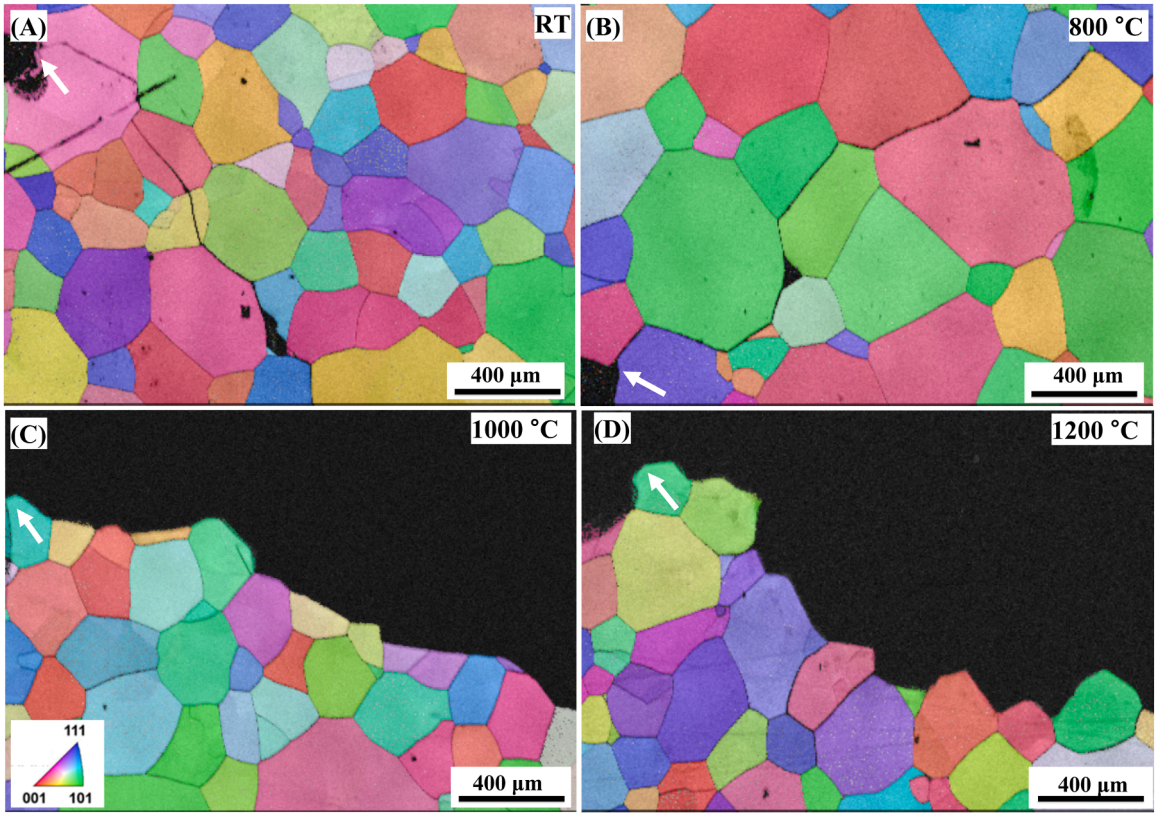

Fig. 8. EBSD inverse pole figure (IPF) maps showing the path of crack propagation in the HT600 compact-tension (C(T)) specimens after the fracture toughness tests at **(A)** RT, **(B)** 800 °C, **(C)** 1000 °C, and **(D)** 1200 °C. The white arrows in the images show the notch tip of the respective C(T) specimens from where the cracks started to propagate. Fracture is predominately intergranular although there is some evidence of transgranular fracture in this structure at RT.

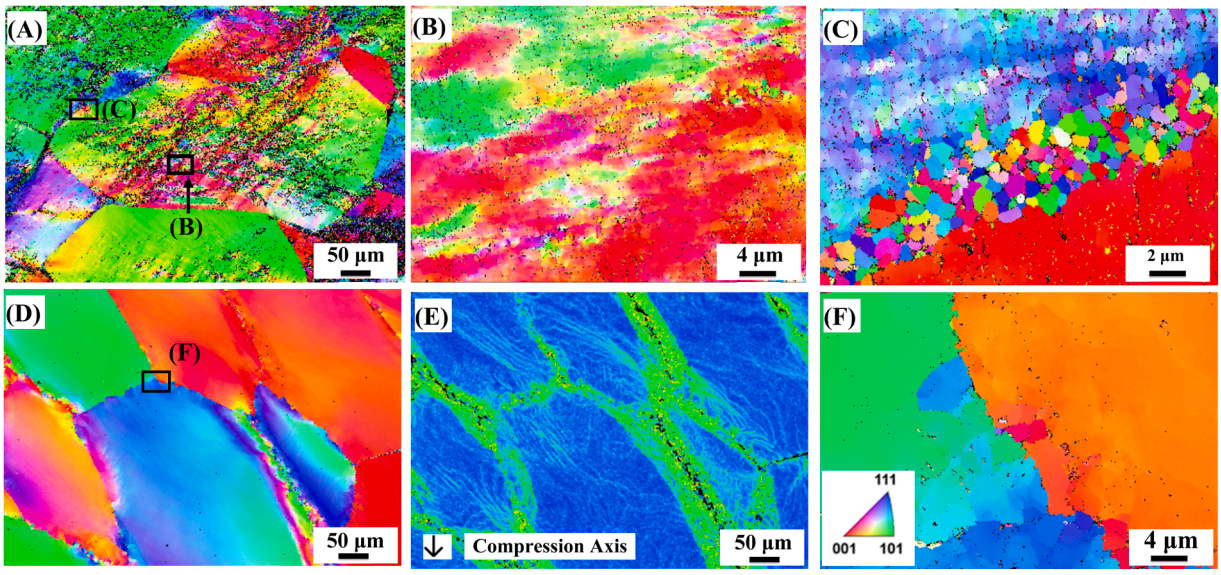

Fig. 9. EBSD inverse pole figure (IPF) maps of the HT600 microstructure after compression testing at 1000 °C. **(A)** A low magnification IPF map showing the representative microstructure of the specimen, **(B)** The magnified IPF map of the interior of a grain obtained from the location indicated in Fig. **A**. (**C**) The magnified IPF map of an area near the grain boundary shown in Fig. **A**. (**D**) Representative IPF map of HT600 microstructure after compression testing at 1200 °C, (**E**) Kernel average misorientation (KAM) map of the location in Fig. **D**. (**F**) IPF map showing recrystallized grains near the grain boundaries from the area indicated inside the Fig. **D**.

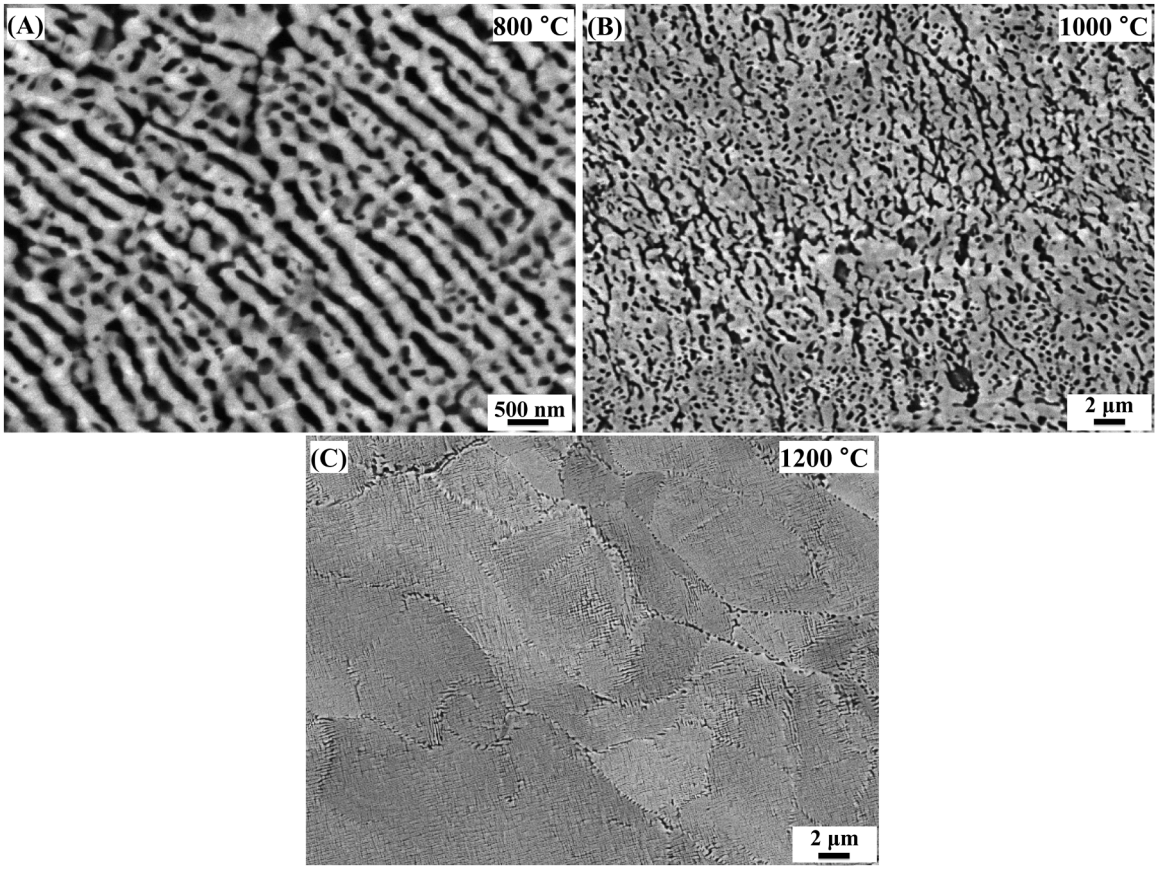

Fig. 10. Representative backscattered electron images of the HT600 microstructure showing the distribution of A2 and B2 phases after compression test at **(A)** 800 °C, **(B)** 1000 °C, and **(C)** 1200 °C.

temperatures. For specimens deformed at 1200 °C, the microstructure consists of small subgrain boundaries possibly decorated with B2 phase or Al-Zr rich precipitates (Fig. 10C). Although the B2 inside the subgrain boundaries is refined at 1200 °C, signifying its progressive dissolution with increasing temperature, the short time exposure during testing is insufficient to complete the B2+A2 → A2 solutionizing reaction. It is

also conceivable that the relatively fine B2 precipitates might have re-formed during the cooling after testing at 1200 °C [17,24]. Interestingly, the BSE microstructure displayed in Fig. 10C consists of three areas with distinct contrast: white, gray, and black. The area with gray contrast indicates the possible formation of the coherent Al-Zr rich precipitate, although this was not confirmed by us [25]. The microstructure with three phases A2, B2, and Al-Zr rich precipitates usually forms due to annealing followed by slow cooling of the alloys with initial A2+B2 microstructures [25,45].

4.2. Grain boundary evolution

The presence of PFZs in the initial microstructures (Fig. 3), shear localization and discontinuous dynamic recrystallization near the grain boundaries during high-temperature compression, and tension-induced intergranular fracture, all point to an essential role of the boundaries during the deformation of the RHSA. First, the microstructure of the undeformed regions (in the grip section of the tensile specimens) was analyzed for each testing condition. Fig. 11A–C show the evolution with temperature of the grain boundaries in these regions for the HT600 condition. As discussed in Section 3.1, the microstructure of HT600 consists of oval-shaped Al-Zr rich grain-boundary precipitates (sized ~1.8 ± 0.7 μm) that are connected by a thin boundary layer of the same intermetallic phase of thickness t ~50 ± 8 nm (Fig. 3B). During tensile testing at 800 °C, the thickness t and volume fraction V_f of this grain-boundary phase remains unchanged; however, its thickness t grew to 94 ± 31 and 274 ± 124 nm, respectively, in the specimens tested at 1000 and 1200 °C. The persistence of the grain-boundary intermetallics signifies their high thermal stability [16,17]. Although the Al-Zr rich precipitates seem to have globularized at 1200 °C, they remain closely spaced along the boundaries; in fact, there is also some evidence of globularization at 1000 °C for the precipitates located at triple junctions (Fig. 11B). Based on our TEM-EDS analysis of the HT600 specimen exposed to 1200 °C, the Al-Zr rich precipitates consist of (at%) 32% Zr, 24% Ta, 15% Al, 11% Ti, and 3.5% O. However, O and N is uniformly distributed everywhere in the microstructure as seen from Fig. 12G and H.

When the HT800 structure is exposed to temperatures of 800 to 1200 °C, the initial fragmented, small, oval-/rod-shaped Al-Zr rich precipitates (Fig. 3D) transform into a continuous thick network throughout the grain boundaries with a thickness t that varies from 4 ± 0.93 to 2.4 ± 0.54 and 5.9 ± 1.5 μm at respective temperatures of 800, 1000, and 1200 °C (Fig. 11D–F). Interestingly, the shape of the intragrain Al-Zr precipitates changes from oval to a rod to oval again with increasing temperature. Initially, the volume fraction V_f of Al-Zr rich precipitate in both the HT600 and HT800 specimens is ~0.6%. With increasing temperatures, the volume fraction V_f of Al-Zr intermetallics in HT800 microstructure changes from ~12% at 800 °C to 16% and 8% respectively at 1000 and 1200 °C. Notably, the thickness t of these precipitates is inversely proportional to their overall volume fraction V_f because the volume fraction of intragrain intermetallics compensate for their reduced thickness along the boundary. As such an evolution of the precipitates in this alloy has never been reported, the EDS maps in Figs. S7 and S8, respectively for specimens tested at 800 and 1000 °C, were used to confirm that these inter- and intra-grain phases were all Al-Zr rich precipitates. Indeed, there was no preferential segregation of O and N observed in these microstructures. Furthermore, for the HT800 microstructures tested at 1200 °C (Fig. 13A–F), the Al-Zr rich precipitates along the grain-boundaries can be seen to be starting to dissolve by rejecting Al at their interface concomitant with the nucleation of the A2 phase inside the boundaries. The line scan across the grain boundary precipitate in this microstructure shows minutely higher O at the precipitate (Fig. S9), although O is expected to be higher on the surface of the thick (~5.9 ± 1.5 μm) precipitate from the high amount of Zr, Nb, and Al that it contains; all these elements have different oxidation tendencies when they are exposed to such high temperatures. Additionally, a mixture of rod- and oval-shaped precipitates of size < 2 μm also formed near the grain boundaries (Fig. 13A); they are also identified by their gray contrast in Fig. 11F. These precipitates have a similar composition to the Al-Zr rich intermetallics. In view of this, both the HT800 and HT600 microstructures consist of A2, B2, and Al-Zr rich precipitates when exposed to 1200 °C (Figs. 12 and 13). Although the Al-Zr rich intermetallics on the grain boundaries start to dissolve at 1200 °C, their thickness t is still larger than that measured at 800 and 1000 °C. As a consequence of this, the width W_{PFZ} ~3 ± 0.7 μm of the PFZs in the 1200 °C microstructure is largest compared to 2.31 ± 0.46 and 1.48 ± 0.27 μm at 800 and 1000 °C, respectively; these microstructures showing the PFZs are given in Fig. S10. As noted above, in the HT800

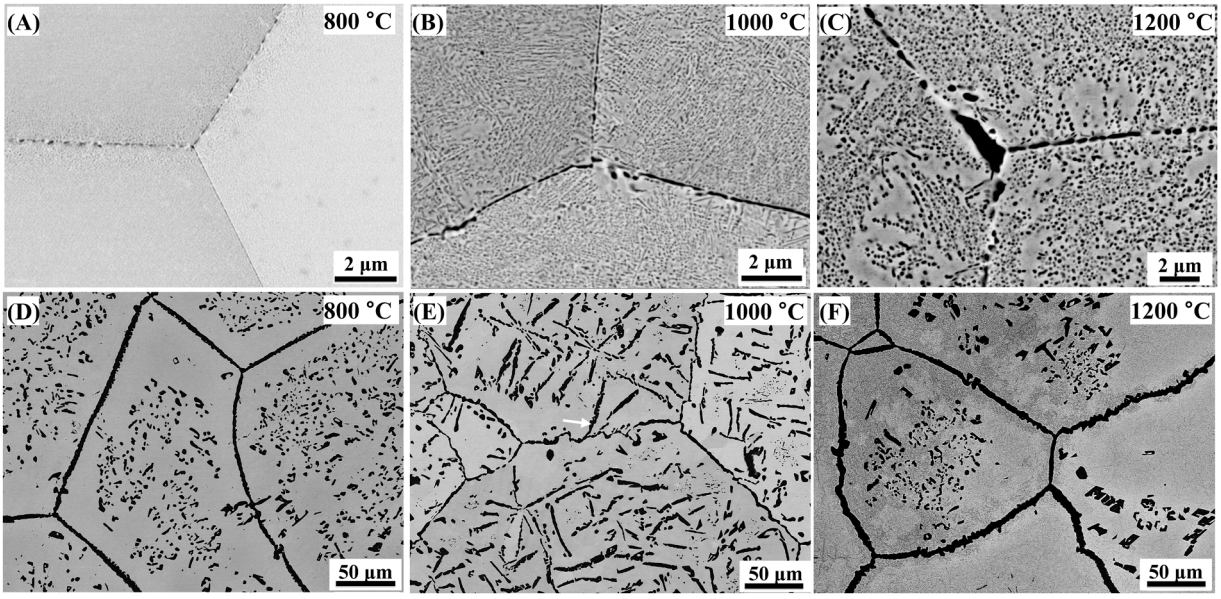

Fig. 11. Representative back-scattered electron images from undeformed regions showing the evolution of grain boundary Al-Zr rich precipitates after they are exposed to temperatures 800 °C, 1000 °C, and 1200 °C during tensile tests in the (A–C) HT600 and (D–F) HT800 microstructures, respectively. The arrow in image **11E** shows the intragrain rod-shaped Al-Zr intermetallic growing from the grain boundary.

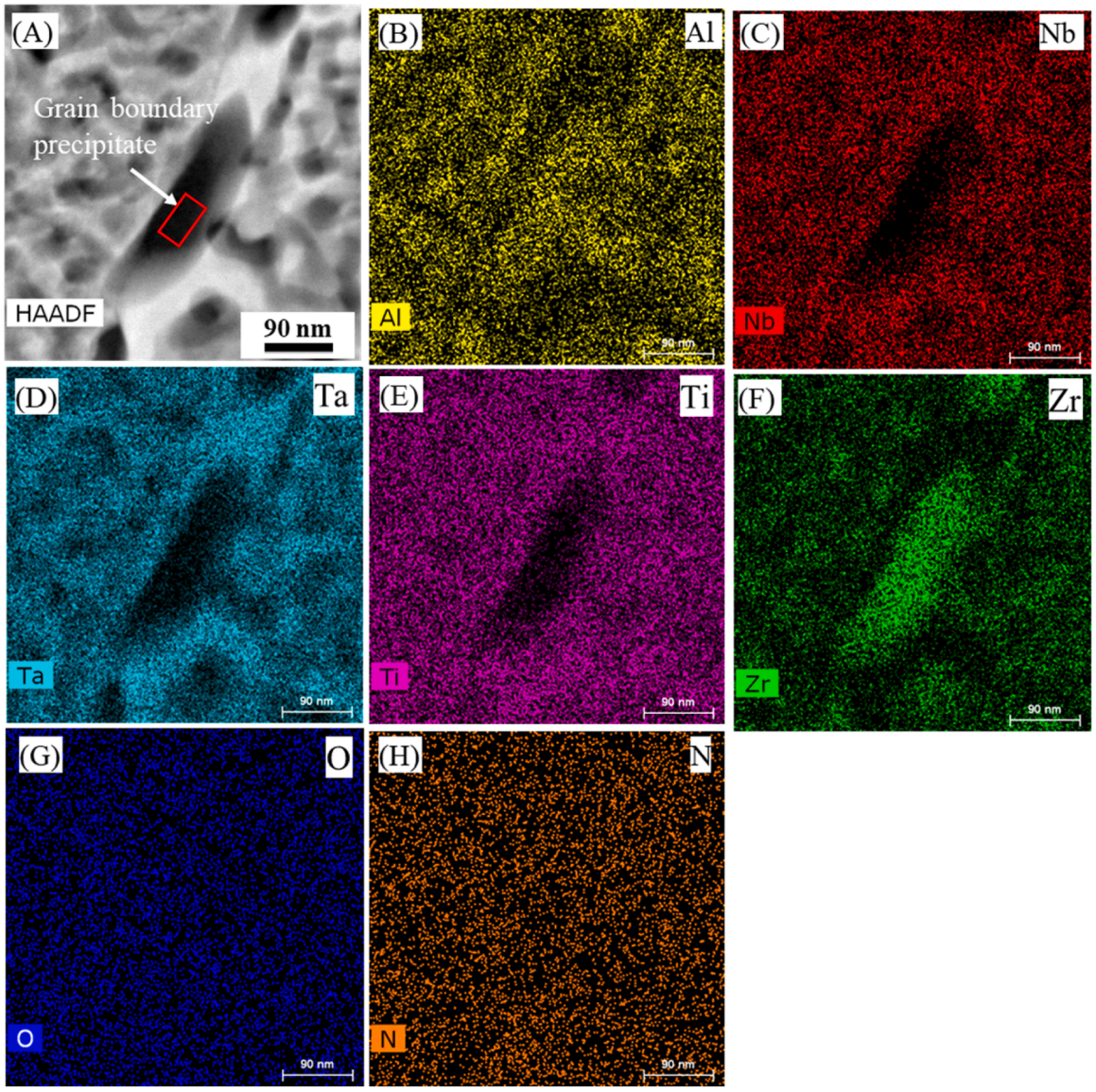

Fig. 12. (A) High-angle annular dark-field scanning transmission electron (HAADF-STEM) image of grain boundary from the undeformed region of the HT600 tensile specimen tested at 1200 °C. The energy dispersive spectroscopy maps show the distribution of elements (B) Al, (C) Ti, (D) Nb, (E) Ta, (F) Zr, (G) O, and (H) N inside the grain boundary and intra-grain precipitates. The red rectangle in (A) shows the location from where the composition of the Al-Zr-rich precipitate was obtained.

microstructure, the thickness of the thin intermetallic boundary layer t, as well as the width W_{PFZ} of the PFZ, first slightly decrease at temperatures from 800 to 1000 °C and then increase again at 1200 °C. In contrast, both t and W_{PFZ} monotonically increase with increasing test temperature in the HT600 microstructure. The presence of these precipitate-free zones have a substantial and detrimental effect on resistance to fracture in this alloy, as described below.

4.3. Fracture behavior

In single-phase *bcc* alloys, intergranular failure is primarily caused by the segregation of interstitial solute atoms or impurities at the grain boundaries. Generally, solute atoms or impurities segregate at the grain boundaries to minimize their strain energy and reduce the grain boundary energy, effectively decreasing atomic cohesion at the grain boundaries to cause intergranular fracture [46,47]. However, if a continuous grain boundary precipitate forms due to microstructural instability, it eliminates the driving force for the segregation of the interstitial solute atoms. This can be further affected by the presence of interstitial impurities although their content in the present RHSA is seemingly too low to seriously affect the alloy's mechanical properties (Table 1).

In precipitate-hardened materials, shear localization in PFZs is known to result in premature failure. For example, in Al and Mg alloys where relatively hard grain-boundary precipitates form during aging, the presence of softer PFZs near the boundaries can lead to intergranular fracture and, as such, significantly diminish strength and toughness [48,49]. In these alloys, the principal mechanism of intergranular fracture is ductile at the micro-scale, *i.e.*, cracks initiate by void nucleation and growth induced by strain localization in the PFZs. For shear localization in PFZs, a relatively softer PFZ compared to the precipitates and the matrix is required. The nano-indentation hardness of the grain boundary Al-Zr rich precipitates in the HT800 microstructure exposed to 1000 °C is ~18.2 ± 0.34 GPa, nearly two times higher than the hardness of the PFZs (Fig. S11). Furthermore, the hardness in the center of the grains is 14% higher compared to the PFZ. A low hardness is expected in both the HT800 and HT600 microstructures since the PFZs in both conditions have a similar composition. In case of shear localization in PFZs, the fracture strain ε_f under tensile loading is proportional to the width of the PFZ W_{PFZ} [43–45]. With reference to the current RHSA, the variation in

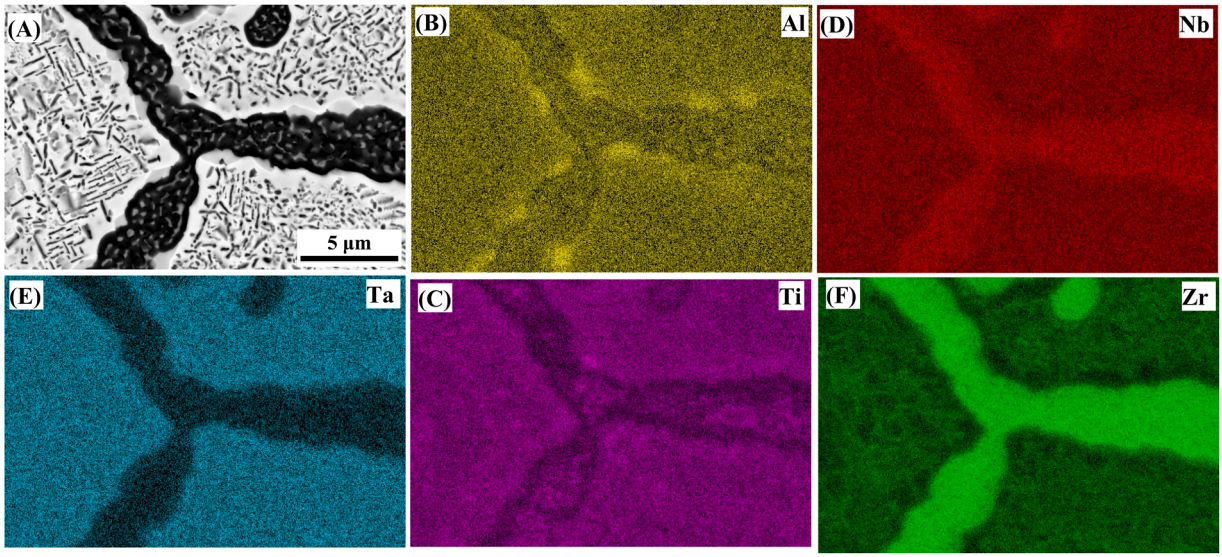

Fig. 13. **(A)** Backscattered electron image of a grain boundary triple point from the undeformed region of the HT800 microstructures tensile tested at 1200 °C. The energy dispersive spectroscopy maps show the distribution of elements **(B)** Al, **(C)** Ti, **(D)** Nb, **(E)** Ta, and **(F)** Zr inside the grain boundary Al-Zr rich precipitate.

measured tensile fracture strain ε_f as a function of W_{PFZ} is shown in Fig. 14 for all tested specimens. It is evident that: (i) all data points for the HT800 microstructure and the data for the HT600 microstructure at elevated temperatures show a linear relationship between ε_f and W_{PFZ}; this indicates that the mechanism of fracture involves nominally ductile shear localization in the PFZ in all cases, except for HT600 microstructure tested at RT where a small proportion of transgranular fracture is evident (Figs. 6A and 8A). (ii) In both the HT600 and HT800 conditions, the values of ε_f decreases and W_{PFZ} increases with increasing temperature, similar to trends observed in Al alloys when grain-boundary precipitates coarsen with increasing aging temperature [49]. Further, in the HT800 condition, the ε_f fracture strain dropped relatively sharply compared to that in HT600. We find that with increasing temperature, the grain-boundary intermetallics in the HT800 microstructure coarsen significantly (Fig. 11), which provides more crack nucleation sites that promote early failure [42,43]. (iii) In the RT condition, the HT800 microstructure follows a linear relationship between ε_f and W_{PFZ}, which

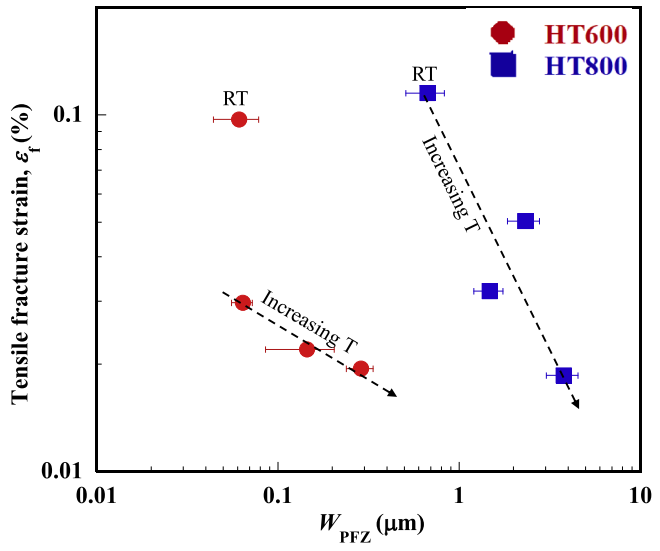

Fig. 14. Variation of tensile fracture strain (ε_f) with the half-width W_{PFZ} of the precipitate-free zone formed near the grain boundaries in the respective HT600 and HT800 microstructures. The arrows indicate the direction of testing temperatures increasing from RT to 1200 °C.

reflects the inherent RT ductility observed in HT800 microstructure under compression. However, this is not the case for the HT600 microstructure; RT HT600 specimens fail prior to general yielding under tensile loading predominately by a brittle intergranular fracture with minor evidence of transgranular fracture, possibly associated with crack initiation from processing induced flaws present near or along the grain boundaries.

Post facto images from the center of the HT600 tensile specimens tested at 1000 °C show the different stages of void nucleation and growth within the PFZ, respectively at locations I, III and II, IV in Fig. 15. Similar mechanisms can be observed within the PFZ in the HT800 specimens tested at 1000 °C, as displayed in region I of Fig. 16, although a transgranular crack can also be observed in region II of Fig. 16A, likely due to crack extension along the rod-shaped Al-Zr rich precipitates growing from the grain boundary into the intra-grain areas, as illustrated by the arrow in Fig. 11E.

Since all the specimens fractured predominately in an intergranular manner in our toughness tests, we believe that such void nucleation and growth by shear localization within PFZ is the primary mechanism of fracture in this alloy. For such fracture within the PFZ, Hahn and Rosenfield have developed a relationship between the fracture toughness and the width of the PFZ, specifically $K_{Ic} \propto W_{PFZ}^{1/2}$ [50,51] the details of which are given in the Supplementary Information. However, the plot in Fig. S9 of the measured K_{Ic} vs. $W_{PFZ}^{1/2}$ in the current RHSA shows no obvious relationship between these two parameters. In fact, the K_{Ic} toughness does not change even after two orders of magnitude increase in $W_{PFZ}^{1/2}$, we believe because a continuous layer of Al-Zr intermetallic is invariably present along the grain boundaries (Figs. 3 and 11) which promotes intergranular fracture within the PFZ [46,47]. The initial HT800 microstructure, however, is somewhat different as the distribution of the grain-boundary intermetallic phase is discontinuous; the RT fracture in this condition is still intergranular but with a significant larger K_{Ic} toughness.

5. Summary and conclusions

This work pertains to an investigation of the compressive, tensile, and fracture toughness of a $Al_{0.5}Nb_{1.25}Ta_{1.25}TiZr$ alloy, from a new class of high-temperature structural materials which have been called refractory high-entropy superalloys. Based on an experimental study of two distinct microstructures in this RHSA, namely a B2 matrix with A2

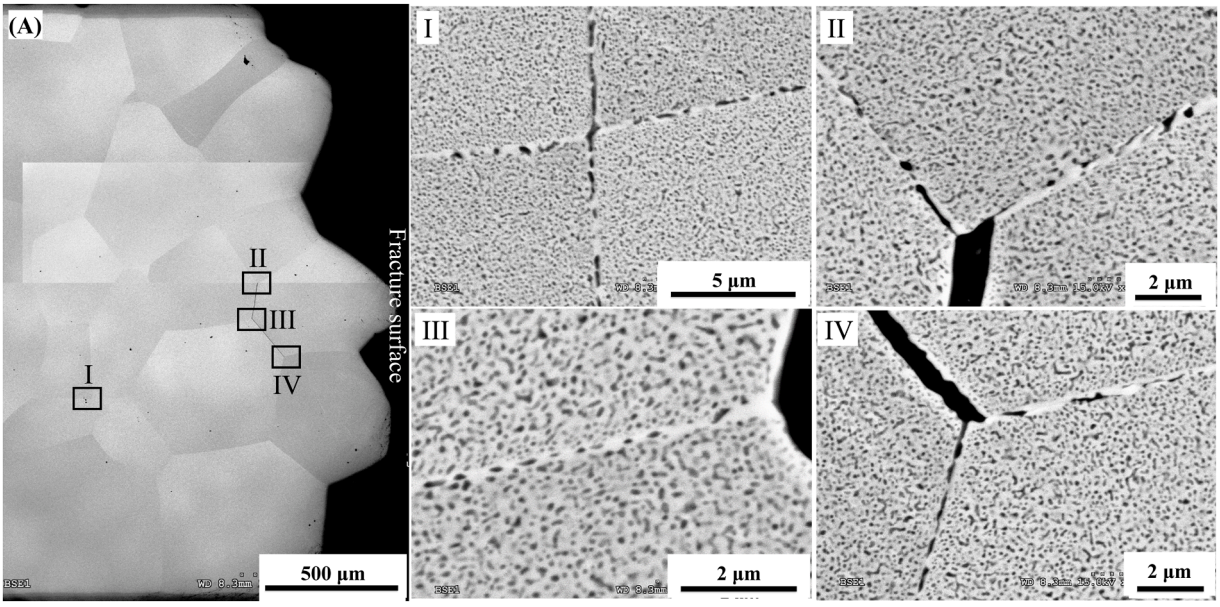

Fig. 15. **(A)** Collage of back-scattered electron images from near the fracture surface of the HT600 tensile specimen tested at 1000 °C. Intergranular cracks below the fracture surface expose the fracture mechanism steps such as crack initiation by void nucleation (at locations **I** and **III**) and crack growth by void coalescence (at locations **II** and **IV**) in the precipitate-free zone near the grain boundaries.

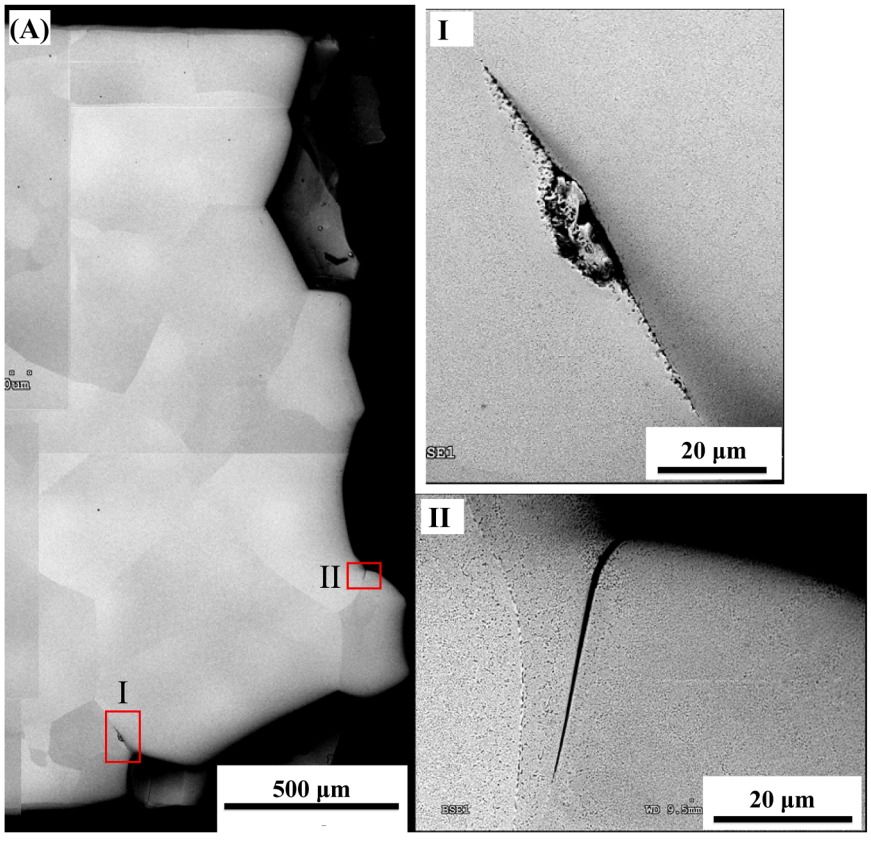

Fig. 16. **(A)** Collage of scanning electron microscope images from near the fracture surface of the HT800 tensile specimen tested at 1000 °C. The magnified image from area **I** shows the crack initiation by void nucleation, and the image from site **II** shows a transgranular crack growth inside the grain.

precipitates (termed HT600) and an A2 matrix with B2 precipitates (termed HT800), which were examined over the temperature range from ambient (RT) to 1200 °C, the following key conclusions can be drawn:

(i) In this RHSA, microstructural design to improve plasticity and generate high ductility measured in compression does not translate to enhanced ductility under tensile loading. Specifically, the alloy displays a plastic strain in excess of 35% under compression at temperatures above 800 °C with strength levels approaching

700 MPa. However, under tensile loading, ductilities are typically 1 to 2 orders of magnitude lower with measured peak strengths in the elastic regime. During tensile deformation, because of shear localization in precipitate-free zones along the grain boundaries from the formation of a generally continuous layer of Al-Zr rich boundary precipitates, all microstructures in this alloy fractured at temperatures from ambient to 1200 °C in a fully intergranular mode.

(ii) The Al-Zr rich precipitates provide an easy path for crack growth along the grain boundaries resulting in low fracture toughness values of $K_{Ic} < 5$ MPa$\sqrt{m}$). However, the K_{Ic} toughness was found to be distinctly improved when the grain-boundary precipitates became globularized and hence are discontinuous.

(iii) Based on this study's findings, there are few considerations worthy of future research and development of the RHSA class of alloys: (a) The formation of Al-Zr rich precipitates along grain boundaries are highly detrimental for the uniaxial tensile and fracture toughness properties of these alloys; in future alloys the formation of grain-boundary Al-Zr precipitates should be avoided. (b) The microstructures in this presently developed RHSA are not stable at elevated temperatures (>800 °C), such that the resulting microstructural degradation leads to poor mechanical properties at elevated temperatures that can severely limit the future application of these alloys. (c) The stark differences between compressive and tensile behavior of RHSA observed in the present study highlight the importance of investigating these materials in tension. Unfortunately, much of the mechanical property results for refractory high-entropy alloys that have been performed to date are for compressive loading, with very limited tensile and fracture toughness data available. For the selection and design of any future, safety-critical high-strength structural alloys, uniaxial tensile and fracture toughness studies are essential.

Declaration of Competing Interest

The authors declare that they have no known competing financial interests or personal relationships that could have appeared to influence the work reported in this paper.

Acknowledgments

This work was primarily supported by the U.S. Department of Energy, Office of Science, Office of Basic Energy Sciences, Materials Sciences and Engineering Division under contract no. DE-AC02-05-CH11231 to the Damage-Tolerance in Structural Materials Program (KC13) at the Lawrence Berkeley National Laboratory (LBNL). S.J.K., J. Y.K., and E.S.P. were supported by Creative Materials Discovery Program through the National Research Foundation of Korea (NRF) funded by Ministry of Science and ICT (no. NRF-2019M3D1A1079215), the Ministry of Trade, Industry & Energy (MOTIE, Korea) under Industrial Technology Innovation Program (No. 10076474). EBSD and TEM microscopy was carried out at LBNL's Molecular Foundry supported by the Office of Science, Office of Basic Energy Sciences, of the U.S. Department of Energy under contract no. DE-AC02-05-CH11231.

Supplementary materials

Supplementary material associated with this article can be found, in the online version, at doi:10.1016/j.actamat.2022.118620.

References

[1] R.O. Ritchie, The conflicts between strength and toughness, Nat. Mater. 10 (2011) 817–822, https://doi.org/10.1038/nmat3115.

[2] R.O. Ritchie, Toughening materials: enhancing resistance to fracture, Philos. Trans. R. Soc. A Math. Phys. Eng. Sci. 379 (2021), 20200437, https://doi.org/10.1098/rsta.2020.0437.

[3] J.H. Perepezko, The hotter the engine, the better, Science 326 (2009) 1068–1069, https://doi.org/10.1126/SCIENCE.1179327 (1979).

[4] R. Raj, M.F. Ashby, Intergranular fracture at elevated temperature, Acta Metall. 23 (1975) 653–666, https://doi.org/10.1016/0001-6160(75)90047-4.

[5] B. Cantor, I.T.H. Chang, P. Knight, A.J.B. Vincent, Microstructural development in equiatomic multicomponent alloys, Mater. Sci. Eng. A 375–377 (2004) 213–218, https://doi.org/10.1016/j.msea.2003.10.257.

[6] J.W. Yeh, S.K. Chen, S.J. Lin, J.Y. Gan, T.S. Chin, T.T. Shun, C.H. Tsau, S.Y. Chang, Nanostructured high-entropy alloys with multiple principal elements: novel alloy design concepts and outcomes, Adv. Eng. Mater. 6 (2004) 299–303, https://doi.org/10.1002/adem.200300567.

[7] O.N. Senkov, G.B. Wilks, J.M. Scott, D.B. Miracle, Mechanical properties of $Nb_{25}Mo_{25}Ta_{25}W_{25}$ and $V_{20}Nb_{20}Mo_{20}Ta_{20}W_{20}$ refractory high entropy alloys, Intermetallics 19 (2011) 698–706, https://doi.org/10.1016/J.INTERMET.2011.01.004 (Barking).

[8] E.P. George, D. Raabe, R.O. Ritchie, High-entropy alloys, Nat. Rev. Mater. 4 (2019) 515–534, https://doi.org/10.1038/s41578-019-0121-4.

[9] D.B. Miracle, O.N. Senkov, A critical review of high entropy alloys and related concepts, Acta Mater. 122 (2017) 448–511, https://doi.org/10.1016/j.actamat.2016.08.081.

[10] O.N. Senkov, D.B. Miracle, K.J. Chaput, J.P. Couzinie, Development and exploration of refractory high entropy alloys-a review, J. Mater. Res. 33 (2018) 3092–3128, https://doi.org/10.1557/jmr.2018.153.

[11] D.B. Miracle, M.H. Tsai, O.N. Senkov, V. Soni, R. Banerjee, Refractory high entropy superalloys (RSAs), Scr. Mater. 187 (2020) 445–452, https://doi.org/10.1016/j.scriptamat.2020.06.048.

[12] O.N. Senkov, D. Isheim, D.N. Seidman, A.L. Pilchak, Development of a refractory high entropy superalloy, Entropy 18 (2016), https://doi.org/10.3390/e18030102.

[13] V. Soni, B. Gwalani, T. Alam, S. Dasari, Y. Zheng, O.N. Senkov, D. Miracle, R. Banerjee, Phase inversion in a two-phase, BCC+B2, refractory high entropy alloy, Acta Mater. 185 (2020) 89–97, https://doi.org/10.1016/J.ACTAMAT.2019.12.004.

[14] V. Soni, O.N. Senkov, B. Gwalani, D.B. Miracle, R. Banerjee, Microstructural design for improving ductility of an initially brittle refractory high entropy alloy, Sci. Rep. 8 (2018) 8816, https://doi.org/10.1038/s41598-018-27144-3.

[15] J.P. Couzinié, M. Heczko, V. Mazánová, O.N. Senkov, M. Ghazisaeidi, R. Banerjee, M.J. Mills, High-temperature deformation mechanisms in a BCC+B2 refractory complex concentrated alloy, Acta Mater. 233 (2022), 117995, https://doi.org/10.1016/j.actamat.2022.117995.

[16] T.E. Whitfield, E.J. Pickering, L.R. Owen, O.N. Senkov, D.B. Miracle, H.J. Stone, N. G. Jones, An assessment of the thermal stability of refractory high entropy superalloys, J. Alloy. Compd. 857 (2021), https://doi.org/10.1016/j.jallcom.2020.157583.

[17] T.E. Whitfield, H.J. Stone, C.N. Jones, N.G. Jones, Microstructural degradation of the AlMo0.5NbTa0.5TiZr refractory metal high-entropy superalloy at elevated temperatures, Entropy 23 (2021) 1–14, https://doi.org/10.3390/E23010080.

[18] T.H. Becker, P. Kumar, U. Ramamurty, Fracture and fatigue in additively manufactured metals, Acta Mater. 219 (2021), 117240, https://doi.org/10.1016/j.actamat.2021.117240.

[19] ASTM International, ASTM E8/E8M standard test methods for tension testing of metallic materials 1, Annual Book of ASTM Standards 4 (2010) 1–27, https://doi.org/10.1520/E0008.

[20] ASTM E399 12, Standard Test Method for Linear-Elastic Plane-Strain Fracture Toughness KIC of Metallic Materials, 3, ASTM International, 2012, https://doi.org/10.1520/E0399-12E03.

[21] ASTM Standard, E1820: measurement of fracture toughness. Annual Book of ASTM Standards, ASTM International, 2003, p. 46.

[22] Z.T. Kloenne, J.P. Couzinié, M. Heczko, R. Gröger, G.B. Viswanathan, W.A.T. Clark, H.L. Fraser, On the bcc/B2 interface structure in a refractory high entropy alloy, Scr. Mater. 223 (2023), 115071, https://doi.org/10.1016/J.SCRIPTAMAT.2022.115071.

[23] M. Akhlaghi, T. Steiner, S. Ramudu Meka, E.J. Mittemeijer, Misfit-induced changes of lattice parameters in two-phase systems: coherent/incoherent precipitates in a matrix, J. Appl. Cryst. 49 (2016) 69–77, https://doi.org/10.1107/S1600576715022608.

[24] O.N. Senkov, S.V. Senkova, C. Woodward, Effect of aluminum on the microstructure and properties of two refractory high-entropy alloys, Acta Mater. 68 (2014) 214–228, https://doi.org/10.1016/j.actamat.2014.01.029.

[25] S. Dasari, A. Sharma, V. Soni, Z. Kloenne, H. Fraser, R. Banerjee, Crystallographic and compositional evolution of ordered B2 and disordered BCC phases during isothermal annealing of refractory high-entropy alloys, Microsc. Microanal. (2022) 1–11, https://doi.org/10.1017/S1431927622012053.

[26] P. Wanjara, M. Jahazi, H. Monajati, S. Yue, J.P. Immarigeon, Hot working behavior of near-α alloy IMI834, Mater. Sci. Eng. A 396 (2005) 50–60, https://doi.org/10.1016/J.MSEA.2004.12.005.

[27] X. Wu, Review of alloy and process development of TiAl alloys, Intermetallics 14 (2006) 1114–1122, https://doi.org/10.1016/J.INTERMET.2005.10.019 (Barking).

[28] F. Liu, J. Chen, J. Dong, M. Zhang, Z. Yao, The hot deformation behaviors of coarse, fine and mixed grain for Udimet 720Li superalloy, Mater. Sci. Eng. A 651 (2016) 102–115, https://doi.org/10.1016/J.MSEA.2015.10.099.

[29] O.N. Senkov, J.M. Scott, S.V. Senkova, F. Meisenkothen, D.B. Miracle, C. F. Woodward, Microstructure and elevated temperature properties of a refractory

TaNbHfZrTi alloy, J. Mater. Sci. 47 (2012) 4062–4074, https://doi.org/10.1007/s10853-012-6260-2.
[30] O.N. Senkov, J.M. Scott, S.v. Senkova, D.B. Miracle, C.F. Woodward, Microstructure and room temperature properties of a high-entropy TaNbHfZrTi alloy, J. Alloy. Compd. 509 (2011) 6043–6048, https://doi.org/10.1016/j.jallcom.2011.02.171.
[31] B.P. Bewlay, M.R. Jackson, J.C. Zhao, P.R. Subramanian, M.G. Mendiratta, J. J. Lewandowski, Ultrahigh-temperature Nb-silicide-based composites, MRS Bull. 28 (2003) 646–653, https://doi.org/10.1557/mrs2003.192.
[32] P. Jéhanno, H. Kestler, A. Venskutonis, M. Böning, M. Heilmaier, B. Bewlay, M. Jackson, Assessment of a powder metallurgical processing route for refractory metal silicide alloys, Metall. Mater. Trans. A 36 (2005) 515–523, https://doi.org/10.1007/s11661-005-0165-5.
[33] Z. Gao, J. Yang, Y. Wu, R. Hu, S.L. Kim, Y.W. Kim, A newly generated nearly lamellar microstructure in cast Ti-48Al-2Nb-2Cr alloy for high-temperature strengthening, Metall. Mater. Trans. A 50 (2019) 5839–5852, https://doi.org/10.1007/s11661-019-05491-8.
[34] S.Y. Chen, L. Wang, W.D. Li, Y. Tong, K.K. Tseng, C.W. Tsai, J.W. Yeh, Y. Ren, W. Guo, J.D. Poplawsky, P.K. Liaw, Peierls barrier characteristic and anomalous strain hardening provoked by dynamic-strain-aging strengthening in a body-centered-cubic high-entropy alloy, Mater. Res. Lett. 7 (2019) 475–481, https://doi.org/10.1080/21663831.2019.1658233.
[35] X.J. Fan, R.T. Qu, Z.F. Zhang, Remarkably high fracture toughness of HfNbTaTiZr refractory high-entropy alloy, J. Mater. Sci. Technol. 123 (2022) 70–77, https://doi.org/10.1016/J.JMST.2022.01.017.
[36] D.M. Bahr, W.S. Johnson, Temperature dependent fracture toughness of a single crystal Nickel superalloy, J. ASTM Int. 2 (2005). www.astm.org.
[37] S. Mitao, T. Isawa, S. Tsuyama, Lamellar orientation dependent anisotropy of fracture toughness in γ-base titanium aluminide, Scr. Metall. Mater. 26 (1992) 1405–1410, https://doi.org/10.1016/0956-716X(92)90657-Z.
[38] R. Gnanamoorthy, Y. Mutoh, N. Masahashi, Y. Mizuhara, Fracture toughness of gamma-base titanium aluminides, Metall. Mater. Trans. A 26 (1995) 305–313, https://doi.org/10.1007/BF02664668.
[39] D.M. Dimiduk, Gamma titanium aluminide alloys - an assessment within the competition of aerospace structural materials, Mater. Sci. Eng. A 263 (1999) 281–288, https://doi.org/10.1016/S0921-5093(98)01158-7.
[40] N.N. Guo, L. Wang, L.S. Luo, X.Z. Li, R.R. Chen, Y.Q. Su, J.J. Guo, H.Z. Fu, Hot deformation characteristics and dynamic recrystallization of the MoNbHfZrTi refractory high-entropy alloy, Mater. Sci. Eng. A 651 (2016) 698–707, https://doi.org/10.1016/J.MSEA.2015.10.113.
[41] R.R. Eleti, T. Bhattacharjee, A. Shibata, N. Tsuji, Unique deformation behavior and microstructure evolution in high temperature processing of HfNbTaTiZr refractory high entropy alloy, Acta Mater. 171 (2019) 132–145, https://doi.org/10.1016/J.ACTAMAT.2019.04.018.
[42] Y. Li, F. Pyczak, J. Paul, M. Oehring, U. Lorenz, Z. Yao, Y. Ning, Rafting of γ′ precipitates in a Co-9Al-9 W superalloy during compressive creep, Mater. Sci. Eng. A 719 (2018) 43–48, https://doi.org/10.1016/J.MSEA.2018.02.017.
[43] H. Long, S.R. Bakhtiari, Y. Liu, S. Mao, H. Wei, Y. Chen, A. Li, D. Kong, L. Yan, L. Yang, Z. Zhang, X. Han, A comparative study of rafting mechanisms of Ni-based single crystal superalloys, Mater. Des. 196 (2020), https://doi.org/10.1016/J.MATDES.2020.109097.
[44] M. Kamaraj, Rafting in single crystal nickel-base superalloys-an overview, Sadhana 28 (2003) 115–128, https://doi.org/10.1007/BF02717129.
[45] L.A. Bendersky, W.J. Boettinger, Transformation of BCC and B2 high temperature phases to HCP and orthorhombic structures in the Ti-Al-Nb system. Part II: Experimental TEM study of microstructures, 1993.
[46] L. Li, R.D. Kamachali, Z. Li, Z. Zhang, Grain boundary energy effect on grain boundary segregation in an equiatomic high-entropy alloy, Phys. Rev. Mater. 4 (2020), https://doi.org/10.1103/PhysRevMaterials.4.053603.
[47] J.R. Rice, J.S. Wang, Embrittlement of interfaces by solute segregation, Mater. Sci. Eng. A 107 (1989) 23–40, https://doi.org/10.1016/0921-5093(89)90372-9.
[48] A. Zindal, J. Jain, R. Prasad, S.S. Singh, P. Cizek, Correlation of grain boundary precipitate characteristics with fracture and fracture toughness in an Mg-8Al-0.5 Zn alloy, Mater. Sci. Eng. A 706 (2017) 192–200, https://doi.org/10.1016/J.MSEA.2017.09.019.
[49] A.K. Vasudévan, R.D. Doherty, Grain boundary ductile fracture in precipitation hardened aluminum alloys, Acta Metall. 35 (1987) 1193–1219, https://doi.org/10.1016/0001-6160(87)90001-0.
[50] G.T. Hahn, A.R. Rosenfield, Metallurgical factors affecting fracture toughness of aluminum alloys, Metall. Trans. A 6 (1975) 653–668, https://doi.org/10.1007/BF02672285.
[51] B.Q. Li, A.P. Reynolds, Correlation of grain-boundary precipitates parameters with fracture toughness in an Al-Cu-Mg-Ag alloy subjected to long-term thermal exposure, J. Mater. Sci. 33 (1998) 5849–5853, https://doi.org/10.1023/A:1004426820624.